Buoyancy-thermocapillary convection of volatile fluids under atmospheric conditions

Tongran Qin[a], Željko Tuković[b], Roman O. Grigoriev[c]

[a]George W. Woodruff School of Mechanical Engineering, Georgia Institute of Technology, Atlanta, GA 30332-0405, USA
[b]University of Zagreb, Faculty of Mechanical Engineering and Naval Architecture, Ivana Lučića 5, Zagreb, Croatia
[c]School of Physics, Georgia Institute of Technology, Atlanta, GA 30332-0430, USA

Abstract

Convection in a layer of fluid with a free surface due to a combination of thermocapillary stresses and buoyancy is one of the classic problems of fluid mechanics. Although extensively studied, it is still not fully understood. In particular, neither the effect of phase change nor the thermal boundary conditions at the liquid-vapor interface have been properly described. These two intimately related issues have a significant impact on the stability of the flow and transitions between different convective patterns. The objective of this paper is to develop and validate a comprehensive numerical model which properly describes both heat transfer and phase change at the liquid-vapor interface, as well as the transport of heat and vapor in the gas layer, which is ignored by the vast majority of theoretical studies with minimal justification. We present a numerical investigation of convection in a long cell filled with a volatile fluid and air, and investigate the changes in convective patterns due to with changes in the applied horizontal temperature gradient. We also explore how variations in the wetting properties of the fluid and lateral confinement (three-dimensionality) affect the flow. While the numerical results have been found to be in general agreement with existing experimental observations, we have also discovered an unexpected phenomenon: a region of evaporation near the cold wall and a region of condensation near the hot wall.

Keywords:
Buoyancy-thermocapillary convection, buoyancy-Marangoni convection, free surface flow, flow instability, thermocapillarity, two phase flow, phase change, numerical simulation

1. Introduction

The flow patterns and dynamic behaviors of liquid films driven by thermocapillarity have attracted the attention of researchers for many years. Initially the interest was driven by applications to crystal growth in microgravity environments, with the focus on liquid metals and, correspondingly, low values of the Prandtl number Pr (typically $Pr < 0.05$). Smith and Davis [1, 2] were the first to perform a linear stability analysis of thermocapillary (or Marangoni) convection in a laterally unbounded liquid layer subject to a horizontal temperature gradient. Ignoring buoyancy effects, they predicted that the return-flow basic state would undergo an instability towards either surface waves (for $Pr < 0.15$) or hydrothermal waves (for $Pr > 0.15$) above a critical Marangoni number Ma, which characterizes the magnitude of thermocapillary stresses. In particular, hydrothermal waves were predicted to travel in the direction of the thermal gradient. Their predictions have since been thoroughly tested and verified both in microgravity and for thin films in terrestrial conditions. A thorough overview of these experiments is presented in a review paper by Schatz and Neitzel [3].

More recently the motivation for further studies of this problem has shifted rather dramatically due to the increased demands on the performance of various cooling technologies. Thermal management is a major issue for a wide range of applications. Many of the modern cooling technologies exploit the large latent heats associated with phase change at the free surface of volatile liquids, allowing compact devices to handle very high heat fluxes. The basic geometry of such cooling devices is similar to the problem investigated under microgravity – a liquid film on the walls of a sealed cavity, under its own vapor as well as noncondensable gases, such as air. Heating one end of the cavity, and cooling the other, establishes a horizontal temperature gradient that drives the flow. However, in addition to thermocapillarity, under terrestrial conditions one often has to consider body forces such as gravity and hence buoyancy. The relative importance of buoyancy and thermocapillarity is quantified by the ratio of Rayleigh and Marangoni numbers $Bo = Ra/Ma$, referred to as the dynamic Bond number.

The first systematic study of buoyancy-thermocapillary convection was performed by Villers and Platten [4] who studied convection in acetone ($Pr = 4.24$) experimentally and numerically using a one-sided model that ignored heat and mass transfer in the gas phase. For low Ma they found the same featureless return flow that characterizes pure thermocapillary convection. However, as Ma was increased, they discovered that the convective patterns which emerge when $Bo = O(1)$ differ substantially from the case dominated by thermocapillarity ($Bo \ll 1$). Instead of hydrothermal waves, they found a steady flow featuring multiple convection rolls. These rolls were found to rotate in the same direction, unlike the case of pure buoy-

ant (or Rayleigh-Bénard) convection. Moreover, unlike the hydrothermal waves which form at an angle to the direction of the thermal gradient, the steady multicellular state features rolls that align in the transverse direction. At even higher Ma the steady state was found to be replaced by an oscillatory multicellular pattern that was also unlike a hydrothermal wave. The convection rolls were observed to travel in the direction opposite to hydrothermal waves.

Similar results were obtained later by De Saedeleer *et al.* [5] for decane ($Pr = 15$) and Garcimartin *et al.* [6] for decane and 0.65 cSt and 2.0 cSt silicone oil ($Pr = 10$ and 30, respectively) in cavities with strong confinement in the spanwise direction. Riley and Neitzel [7] performed one of the most extensive and detailed experimental studies of convection in a 1 cSt silicone oil with $Pr = 13.9$ in a rectangular cavity with a spanwise dimension comparable to the streamwise dimension. They discovered that a direct transitions from steady, unicellular flow to hydrothermal waves takes place for small values of the dynamic Bond number ($Bo \lesssim 0.2$), while for $Bo \gtrsim 0.2$ the results are similar to those of Refs. [4, 5, 6]: first a transition to steady co-rotating multicells, and upon further increase in Ma, to an oscillatory multicellular pattern. Riley and Neitzel also determined the critical values of Ma and the wavelength λ of the convective pattern as a function of Bo.

The linear stability analysis of Smith and David [1] provides an accurate description of experimentally observed convective patterns for low Bo. However, it fails to predict the patterns that emerge for $Bo = O(1)$, although the spatially uniform return flow at low Ma is found to be consistent [7] with the analytical solution for the velocity and temperature [8, 9] away from the lateral boundaries. The majority of the studies that have performed linear stability analysis around this analytical solution ignore the effect of the end walls and, hence, predict incorrect patterns. In particular, for adiabatic boundary conditions at the top and bottom of the liquid layer, Parmentier *et al.* [10] predict transition to traveling waves rather than steady multicellular pattern for $Pr \leq 7$ fluids regardless of the value of Bo. Chan and Chen (2010), who used similar assumptions, also predict transition to traveling waves for a $Pr = 13.9$ fluid. Moreover their critical Ma and wavelength λ do not match the experiment [7]. In both cases the traveling waves are oblique for smaller Bo and become transverse for $Bo > Bo_c = O(1)$.

Mercier and Normand [11] showed that transition to a stationary convective pattern can take place if the adiabatic boundary conditions are replaced with Newton's cooling law, although that requires an unrealistically large surface Biot number ($Bi \gtrsim 185/Bo$). Moreover, the predicted pattern corresponds to longitudinal convection rolls, while in the experiments [4, 5, 6, 7] transverse rolls were observed. In a subsequent paper Mercier and Normand [12] considered the effects of the end walls, which they described as spatial disturbances superimposed on the uniform base flow. It was found that depending upon the Prandtl number, recirculation rolls would develop near the hot end ($Pr > 4$), near the cold end ($Pr < 0.01$) or at both end walls ($0.01 < Pr < 4$).

Priede and Gerbeth [13] where the first to consider the effect of the end walls on the stability of the base flow. They used a generalized linear stability analysis to argue that hydrothermal waves correspond to a global oscillatory instability which dominates at lower Bo, while the stationary patterns result from a local absolute instability which, for higher Bo, has a lower threshold value of Ma than the global oscillatory instability. Their prediction agrees remarkably well with the threshold values found by Riley and Neitzel [7].

Understanding the convective patterns above the threshold of the primary instability requires a numerical approach. To date, the majority of numerical studies (e.g., Villers and Platten [4], Ben Hadid and Roux [14], Mundrane and Zebib [15], Lu and Zhuang [16], Shevtsova *et al.* [17]) have focused on 2D flows. Furthermore, just like the linear stability analyses, existing numerical studies assume that the temperature gradient is generated by imposing fixed temperatures on the two end walls; the free surface is flat and non-deformable; the thermal boundary conditions on the bottom wall and the interface are either adiabatic or conducting; and phase change is negligible. Unlike the other studies, Ji *et al.* [18] consider the effect of phase change on the thermal boundary condition at the free surface, but they ignore buoyancy.

While the 2D approximation may be appropriate in describing some experiments, the validity of the rest of these assumptions is questionable. Validating them is one of the main objectives of the present study. Furthermore, while the numerical simulations reproduce some features of the experimental studies [4, 5, 6, 7], they fail partially or completely in describing other features, most notably the structure of the boundary layers near the end walls which defines both the temperature gradient in the bulk and controls the dynamics of oscillatory states at higher Ma. Description of these boundary layers requires a detailed model of transport of heat (and mass) in both the liquid and the vapor layer, as well as phase change at their interface.

We present such a model of two-phase flow and its numerical implementation in the following Section. The results obtained using this model in a specific test problem, namely buoyancy-thermocapillary convection in a sealed rectangular cavity where the dimension along the temperature gradient is much greater than the other two dimensions and any evaporation must be balanced by condensation are presented and discussed in Section 3 and our conclusions – in Section 4.

2. Mathematical Model

2.1. Governing Equations

Existing analytical and numerical studies of buoyancy-thermocapillary convection, with rare exceptions, use one-sided models where heat and mass transport in the gas phase are incorporated indirectly through boundary conditions at the liquid-vapor interface. While such an approach might be justifiable for nonvolatile liquids since air is a relatively poor conductor of heat, volatile liquids require a two-sided model. For volatile liquids, phase change can lead to significant heat fluxes in the liquid layer due to the latent heat released or absorbed at the interface. The interfacial mass flux (which defines the heat flux) cannot be computed reliably without a proper model of bulk mass transport in the gas phase.

Two-sided models have been formulated previously by Wang *et al.* [19] for a meniscus in a microtube, by Pan and Wang [20] for a meniscus in an exposed pore, and by Wang *et al.* [21] for an open groove. These models, however, assume rather than compute the shape of the free surface and do not account for the advective transport of heat and mass in the gas phase.

In order to describe convection in both volatile and non-volatile fluids, the heat and mass transport in both phases must be modeled explicitly. Both the liquid and the gas phases can be considered incompressible, since the fluid velocities $\mathbf{u}$ are much smaller than the speed of sound at small length scales. Hence the continuity equation reduces to $\nabla \cdot \mathbf{u} = 0$. Because the fluid velocities can, however, be large enough for inertial effects to be significant, the momentum transport in the bulk should be described by the Navier-Stokes equation

$$\rho\left(\partial_t \mathbf{u} + \mathbf{u} \cdot \nabla \mathbf{u}\right) = -\nabla p + \mu \nabla^2 \mathbf{u} + \rho\left(T\right)\mathbf{g} \tag{1}$$

where p is the fluid pressure, ρ and μ are the fluid's density and viscosity, and $\mathbf{g}$ is the gravitational acceleration.

Following standard practice, we use the Boussinesq approximation, retaining the temperature dependence only in the last term to represent the buoyancy force. This is consistent with the assumption of incompressibility, since the relative change in the density due to temperature variation is usually quite small (less than 10% for the vapor and less than 4% for the liquid in the examples considered below). Specifically, in the liquid phase

$$\rho_l = \rho_l^*[1 - \beta_l\left(T - T^*\right)], \tag{2}$$

where ρ_l^* is the reference density at the reference temperature T^* and $\beta_l = -(\partial\rho_l/\partial T)/\rho_l$ is the coefficient of thermal expansion. Here and below, subscripts l, g, v, a and i denote properties of the liquid and gas phase, vapor and air component, and the liquid-gas interface, respectively. In the gas phase

$$\rho_g = \rho_a + \rho_v, \tag{3}$$

where both vapor ($n = v$) and air ($n = a$) are considered to be ideal gases

$$p_n = \rho_n \bar{R}_n T, \tag{4}$$

$\bar{R}_n = R/M_n$, R is the universal gas constant, and M_n is the molar mass. The total gas pressure is the sum of partial pressures

$$p_g = p_a + p_v. \tag{5}$$

Both equations of state (2) and (4) can be easily generalized as needed. On the left-hand-side of (1) the density is considered constant for each phase (defined as the spatial average of $\rho(T)$).

The Navier-Stokes equation (1) only describes simple fluids or multi-component fluids in the dilute approximation. Although the equations governing momentum transport in multi-component mixtures generalizing the Navier-Stokes equation for a simple fluid are known [13], no efficient numerical solvers for these equations have been developed. Hence, the model is restricted to situations where the dilute approximation is valid in the gas phase, e.g., the molar fraction of air is much greater than that of vapor.

For a volatile fluid in confined geometry, the external temperature gradient causes both evaporation and condensation, with the net mass of the fluid being globally conserved. Conventionally, the mass transport of the less abundant component, i.e., vapor, is described by the advection-diffusion equations for the concentration (defined as the molar fraction) of vapor in the mixture. However, this equation does not guarantee mass conservation. To ensure local mass conservation, we use the advection-diffusion equation for the density of vapor instead,

$$\partial_t \rho_v + \mathbf{u} \cdot \nabla \rho_v = D \nabla^2 \rho_v \tag{6}$$

where D is the diffusion coefficient of vapor in air. As a consequence, the mass of vapor is also conserved globally.

Mass conservation of air, which is a noncondensable gas and the dominant component in the gas phase, requires a separate equation

$$\int_{\text{gas}} \rho_a dV = m_a, \tag{7}$$

where m_a is the total mass of air. The densities of air and vapor are related to their partial pressures through (4). Furthermore, the solution of the Navier-Stokes equation defines the pressure field p up to a constant p_o, so that total pressure is

$$p_g = p + p_o, \tag{8}$$

where the pressure offset p_o can be computed from the mass conservation constraint (7) using (3), (4), (5) and (8):

$$p_o = \left[\int_{\text{gas}} \frac{1}{\bar{R}_a T} dV\right]^{-1} \left[m_a - \int_{\text{gas}} \frac{p - \rho_v \bar{R}_v T}{\bar{R}_a T} dV\right]. \tag{9}$$

The concentration c_v of vapor can be computed from the equation of state using the partial pressure

$$c_v = p_v/p_g \tag{10}$$

while the concentration of air is therefore $c_a = 1 - c_v$. Finally, the transport of heat is also described using an advection-diffusion equation

$$\partial_t T + \mathbf{u} \cdot \nabla T = \alpha \nabla^2 T, \tag{11}$$

where $\alpha = k/\rho C_p$ is the fluid thermal diffusivity, k is the thermal conductivity, and C_p is the heat capacity, of the fluid.

2.2. Boundary Conditions

The system of coupled evolution equations for the velocity, pressure, temperature, and density fields has to be solved in a self-consistent manner, subject to the boundary conditions describing the balance of momentum, heat, and mass fluxes. The phase change at the liquid-gas interface can be described using the Kinetic Theory [22] expression for the mass flux across the interface

$$J = \frac{2\lambda}{2 - \lambda}\sqrt{\frac{1}{2\pi \bar{R}_v}}\left[\frac{p_s(T_i)}{T_i^{1/2}} - \frac{p_v}{T_g^{1/2}}\right], \tag{12}$$

where λ is the accommodation coefficient, which is usually taken to be equal to unity (the convention we follow here) and

subscript s denotes saturation values for the vapor. We used an alternative form of this expression derived by Wayner *et al.* [23] by a Taylor series expansion of (12) about the equilibrium state

$$J = \frac{2\lambda}{2-\lambda}\rho_v\sqrt{\frac{\bar{R}_v T_i}{2\pi}}\left[\frac{p_l - p_g}{\rho_l \bar{R}_v T_i} + \frac{\mathcal{L}}{\bar{R}_v T_i}\frac{T_i - T_s}{T_s}\right], \tag{13}$$

which has been further modified to explicitly incorporate the pressure jump (e.g., due to curvature or disjoining pressure) across the interface. We have verified that (12) and (13) give numerically indistinguishable results.

The local saturation temperature depends on the partial pressure of vapor through the Antoine's equation for phase equilibrium

$$\ln p_v = A_v - \frac{B_v}{C_v + T_s} \tag{14}$$

where A_v, B_v, and C_v are empirical coefficients. The Antoine's equation is a generalization (valid over a wider range of temperatures) of the Clausius-Clapeyron equation

$$\ln\frac{p_v}{p_v^*} = \frac{\mathcal{L}}{\bar{R}_v}\left(\frac{1}{T_s^*} - \frac{1}{T_s}\right), \tag{15}$$

where T_s^* is the saturation temperature at the reference vapor pressure p_v^*. Again, we have verified that the two relations produce indistinguishable results for moderate temperature gradients explored here.

Mass flux balance on the gas side of the interface is given by

$$J = -D\,\mathbf{n}\cdot\nabla\rho_v + \rho_v\,\mathbf{n}\cdot(\mathbf{u}_g - \mathbf{u}_i), \tag{16}$$

where the first term represents the diffusion component, and the second term represents the advection component (referred to as the "convection component" by Wang *et al.* [21]) and $\mathbf{u}_i$ is the velocity of the interface. Since air is noncondensable, its mass flux across the interface is zero, therefore

$$0 = -D\,\mathbf{n}\cdot\nabla\rho_a + \rho_a\,\mathbf{n}\cdot(\mathbf{u}_g - \mathbf{u}_i). \tag{17}$$

For binary diffusion, the diffusion coefficient of vapor through air is the same as that of air through vapor, while the concentration gradients of vapor and air have the same absolute value but opposite direction, which yields the relation between the density gradients of vapor and air

$$\frac{\mathbf{n}\cdot\nabla\rho_v}{\mathbf{n}\cdot\nabla\rho_a} = -\frac{M_v}{M_a}. \tag{18}$$

Combining (14), (16), (17) and (18) with the statement of heat flux balance

$$\mathcal{L}J = \mathbf{n}\cdot k_l\nabla T_l - \mathbf{n}\cdot k_g\nabla T_g \tag{19}$$

we can solve for the mass flux J, the interfacial temperature T_i, the saturation temperature T_s, the normal component of the gas velocity at the interface $\mathbf{n}\cdot\mathbf{u}_g$, the air density ρ_a and the normal component of the density gradient of vapor $\mathbf{n}\cdot\nabla\rho_v$.

The remaining boundary conditions for $\mathbf{u}$ and T at the liquid-vapor interface are standard: the temperature is considered to be continuous

$$T_l = T_i = T_g \tag{20}$$

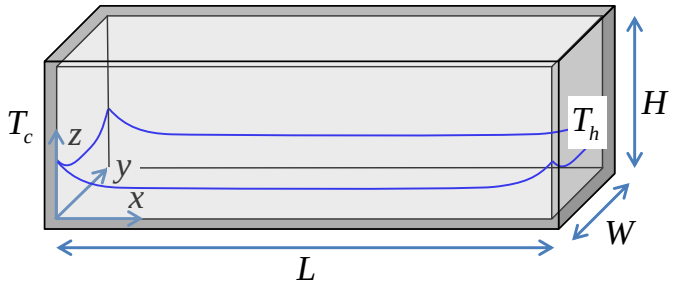

Figure 1: The test cell containing the liquid and air/vapor mixture. Gravity is pointing in the negative z direction. The shape of the contact line reflects the curvature of the free surface.

and so are the tangential velocity components

$$(1 - \mathbf{n}\cdot\mathbf{n})\cdot(\mathbf{u}_l - \mathbf{u}_g) = 0. \tag{21}$$

The normal component of $\mathbf{u}_l$ can be computed using mass balance across the interface. Since the liquid density is much greater than that of the air or vapor,

$$\mathbf{n}\cdot(\mathbf{u}_l - \mathbf{u}_i) = \frac{J}{\rho_l} \approx 0. \tag{22}$$

The stress balance

$$(\Sigma_l - \Sigma_g)\cdot\mathbf{n} = \mathbf{n}\kappa\sigma + \nabla_s\sigma = \mathbf{n}\kappa\sigma - \gamma\nabla_s T_i \tag{23}$$

incorporates both the viscous drag between the two phases and thermocapillary effects. Here $\Sigma = \mu\left[\nabla\mathbf{u} - (\nabla\mathbf{u})^T\right] - p$ is the stress tensor, κ is the interface curvature, $\nabla_s = (1-\mathbf{n}\cdot\mathbf{n})\cdot\nabla$ is the surface gradient, and $\gamma = -\partial\sigma/\partial T$ is the temperature coefficient of surface tension.

We further assume that the fluid is contained in a rectangular test cell with inner dimensions $L \times W \times H$ (see Fig. 1) and thin walls of thickness h_w and conductivity k_w. The left wall is cooled with constant temperature T_c imposed on the outside, while the right wall is heated with constant temperature $T_h > T_c$ imposed on the outside. Since the walls are thin, one-dimensional conduction is assumed, yielding the following boundary conditions on the inside of the side walls:

$$T|_{x=0} = T_c + \frac{k_n}{k_w}h_w\,\mathbf{n}\cdot\nabla T, \tag{24}$$

$$T|_{x=L} = T_h + \frac{k_n}{k_w}h_w\,\mathbf{n}\cdot\nabla T, \tag{25}$$

where $n = g$ ($n = l$) above (below) the contact line.

Heat flux through the top, bottom, front and back walls is ignored (adiabatic boundary conditions are typical of most experiments). Standard no-slip boundary conditions $\mathbf{u} = 0$ for the velocity and no-flux boundary conditions

$$\mathbf{n}\cdot\nabla\rho_v = 0 \tag{26}$$

for the vapor density are imposed on all the walls. The pressure boundary condition

$$\mathbf{n}\cdot\nabla p = \rho(T)\,\mathbf{n}\cdot\mathbf{g} \tag{27}$$

follows from (1).

Field	Types of boundary conditions			
	Interface, vapor side	Interface, liquid side	Hot/Cold walls	Other alone walls
$\mathbf{u}$	Dirichlet	Neumann	Dirichlet	Dirichlet
p	Neumann	Dirichlet	Neumann	Neumann
T	Dirichlet	Neumann	Neumann	Neumann
ρ	Neumann	–	Neumann	Neumann

Table 1: Types of boundary conditions imposed on various boundaries in the numerical implementation of the model.

2.3. Implementation

The model described above has been implemented numerically by adapting an open-source general-purpose CFD package OpenFOAM [24] to solve the governing equations in both 2D and 3D geometries. The types of boundary conditions imposed at different interfaces are summarized in Table 1. For instance, temperature continuity (20) is imposed on the vapor side, while the heat flux balance (19) is imposed on the liquid side of the interface.

Each time step involves three major parts: updating the interface shape and the computational mesh; updating the boundary conditions on the velocity, pressure, temperature and density fields; and updating pressure, velocity, temperature, density and concentration fields in the bulk. Since the shape of the interface, the boundary conditions, and the bulk fields are coupled, these three parts are repeated iteratively, until convergence.

The shape of the liquid-vapor interface is updated using (22) based on the normal component of the velocity $\mathbf{u}_l$ in the liquid phase. We use the surface-tracking method [25] in which the interface coincides with a set of mesh cell faces. Since the computational mesh has to conform to the interface shape at all times, it is being continuously distorted by the interface motion.

In order to solve the governing equations for the bulk fields in the liquid and the vapor domain, the boundary conditions described in the previous Section are updated on both sides of the interface. Since the mass flux J, the interfacial temperature T_i, the saturation temperature T_s, the normal component of the gas velocity, the density fields ρ_a and $\mathbf{n} \cdot \nabla \rho_v$ are coupled, the corresponding boundary conditions are solved iteratively, with bulk fields held constant. Boundary conditions are also updated on all the solid walls.

Once the boundary conditions are updated, bulk pressure, velocity, temperature, density, and concentration fields are computed using the finite volume method [26]. In particular, pressure and velocity are solved for using PISO (Pressure Implicit with Splitting of Operators) algorithm [27], where the velocity field is predicted before the pressure equation is solved so that continuity is satisfied, and velocity is then corrected based on changes in pressure field. It is an iterative procedure repeated until both the pressure and the velocity field converge. Once the velocity field is computed, the temperature, density and concentration fields are updated.

	liquid	gas
μ (kg/m-s)	4.95×10^{-4}	1.82×10^{-5}
ρ (kg/m^3)	761.0	1.43
β (1/K)	1.34×10^{-3}	$1/T$
α (m^2/s)	9.52×10^{-8}	1.89×10^{-5}
Pr	6.83	0.67
σ (N/m)	1.59×10^{-2}	
γ (N/m-K)	7×10^{-5}	
D (m^2/s)	2.5×10^{-5}	
$\mathcal{L}$ (J/kg)	2.14×10^5	

Table 2: Material properties at the reference temperature $T = 293$ K and pressure $p = 1$ atm. In the gas phase, the coefficient of thermal expansion $\beta = 1/T$ based on the ideal gas assumption and the viscosity is taken equal to that of the dominant component (i.e., air).

3. Results and Discussion

In this section, we use the computational model to investigate the buoyancy-thermocapillary flow of a fluid confined in a sealed rectangular test cell used in the experimental study of Li *et al.* [28]. A 0.65 cSt silicone oil, hexamethyldisloxane, which is a volatile liquid with the properties summarized in Table 2, was used as the working fluid. A layer of liquid is confined in the test cell (see Fig. 1) below a layer of gas, which is a mixture of vapor and air, held at ambient pressure. The walls of the test cell are made of quartz (fused silica) with thermal conductivity $k_w = 1.4$ W/m-K and have a thickness $h_w = 1.25$ mm. Silicone oil wets quartz very well, but in the numerics we set the contact angle $\theta = 50°$ (unless noted otherwise) to avoid numerical instabilities.

While the numerical model can describe the flows in both 2D and 3D systems, most of the results presented here are obtained for 2D flows (ignoring variations in the y-direction), since 3D simulations require significantly more computational resources. The 2D system corresponds to the central vertical (x-z) plane of the test cell, with the inner dimensions $L \times H = 48.5$ mm $\times 10$ mm. The 3D system simulated here, however, is smaller in length, width, and height than the experimental test cell.

The nondimensional parameters which determine the flow regimes are conventionally defined in terms of the properties of the liquid layer, its thickness d_l and the gradient of the interfacial temperature $\tau = \partial T_i / \partial x$. If we ignore the effect of the gas phase, the main parameters are the Rayleigh number

$$Ra_l = \frac{g \beta_l d^4 \tau}{\nu_l \alpha_l} \tag{28}$$

characterizing buoyancy, the interfacial Marangoni number

$$Ma_l = \frac{\gamma d_l^2 \tau}{\mu_l \alpha_l} \tag{29}$$

characterizing thermocapillarity, the dynamic Bond number $Bo_l = Ra_l / Ma_l$, and the Prandtl number $Pr_l = \nu_l / \alpha_l$ (where $\nu = \mu / \rho$ is the kinematic viscosity). Occasionally the Grashof number $Gr_l = Ra_l / Pr_l$ and the Reynolds number $Re_l = Ma_l / Pr_l$ are used instead of Ra_l and Ma_l. The geometry is characterized by the streamwise (longitudinal) aspect ratio $\Gamma_x = L / d_l$ and the

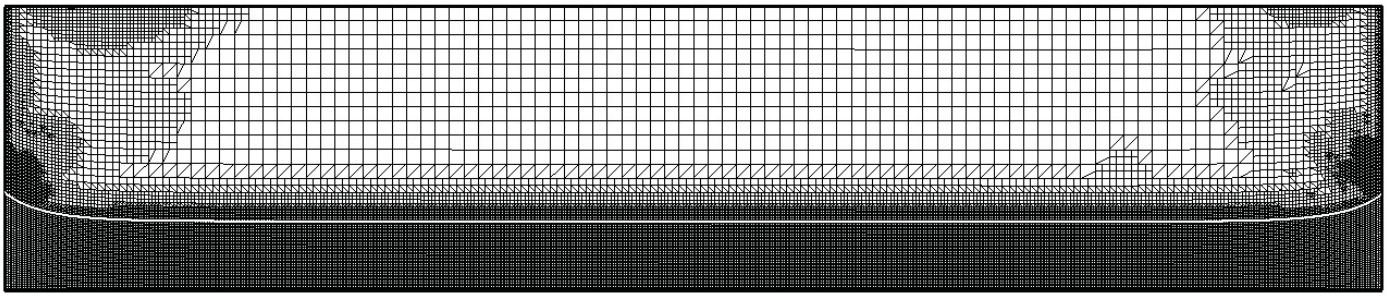

Figure 2: Typical 2D computational mesh showing multiple levels of refinement. All the computational mesh cells are hexahedrons (diagonal lines are rendering artifacts). The largest mesh cell size is 0.5 mm and the smallest mesh cell size is 1/16 mm (= 0.0625 mm). The white solid line indicates the position of the free surface.

spanwise (transverse) aspect ratio $\Gamma_y = W/d_l$. In this study we fix $Pr_l = 6.8$ and $Bo_l = 0.853$, which corresponds to $d_l = 2.45$ mm. Of the five parameters (Ma_l, Bo_l, Pr_l, Γ_x, Γ_y) only Ma_l depends on $\Delta T = T_h - T_c$ (implicitly through the interfacial temperature gradient τ).

Initially, the fluid is assumed stationary with uniform temperature $T_0 = (T_c + T_h)/2$ (we use $T_0 = 293$ K in all cases), the liquid layer is of uniform thickness (such that the liquid-gas interface is flat), and the gas layer is a uniform mixture of the vapor and the air. The partial pressure of the vapor $p_v = p_s(T_0)$ is set equal to the vapor pressure at T_0, calculated from (14), and the partial pressure of air p_a is such that the total pressure p_g is equal to the ambient pressure. As the system evolves towards an asymptotic state, the flow develops in both phases, the interface distorts to accommodate the assigned contact angle at the walls, and gradients in the temperature and vapor concentration are established.

As the shape of the interface evolves, so does the computational mesh. As previous numerical studies [14] discovered, and our simulations confirmed, the size of the mesh cells needs to be small enough to resolve the fine structure of the flow, especially in the liquid layer. For instance, we find that, in order to properly resolve convection rolls in the liquid, the mesh resolution should be at least 1/8 mm (= 0.125 mm). Finer meshes have a greater number of cells and require smaller time steps and, hence, are more computationally expensive. Since the initial transient state is of secondary interest, we let the system relax to the asymptotic state using a coarse hexahedral mesh (initially all cells are cubical with side 0.5 mm).

Once the transient dynamics have died down, the mesh is refined in several steps, until the results become mesh independent. At each level, the mesh is refined uniformly (by splitting each cell in all three directions) in the liquid phase and in the gas phase just above the free surface. Additionally the mesh in the gas phase is refined in the regions (typically near the contact lines) where the second derivatives of the physical fields (pressure, velocity, or temperature) exceed specified thresholds. A typical mesh applied at the final stage of a simulation is shown in Fig. 2. Additional details are provided in the appendix.

To ensure that an asymptotic state (steady or time-periodic) is reached, all the 2D simulations were carried out to a physical time of at least 600 seconds, while the 3D simulations, which were much more computationally intensive, were carried out to physical times of at least 100 seconds. We start by presenting the results of 2D simulations which correspond to replacing the physical boundary conditions on the side walls (front and back of the cavity) with periodic boundary conditions for all the fields.

3.1. Steady Unicellular and Multicellular Flow

For sufficiently low ΔT, the flow eventually reaches a steady state. Fig. 3 shows the streamlines of this steady flow in both the liquid and the gas phases at several values of ΔT. In particular, when $\Delta T = 4$ K, a uniform return-flow basic state is observed in the core region of the flow. The liquid flows from the hot end of the test cell (right) towards the cold end (left) along the free surface, driven by a combination of buoyancy and thermocapillary stresses, with a return flow near the bottom. In the gas layer, thermocapillarity opposes buoyancy, resulting in a large clockwise convective roll in the core region. Buoyancy produces two smaller counterclockwise recirculation rolls in the top corners. Following Riley and Neitzel's terminology, we will call this a steady unicellular flow (SUF).

At $\Delta T = 7$ K several convection rolls emerge in the liquid layer near the hot wall. This pattern corresponds to the steady multicellular flow (SMC). When the temperature difference is increased to $\Delta T = 10$ K, convection rolls become more pronounced, especially near the hot wall, but the pattern still does not extend across the entire cell. This convective motion starts to affect the temperature field, with the waviness of the isotherms in the liquid phase (see Fig. 4) near the hot wall reflecting the convective motion of the fluid. By the time ΔT is increased to 15 K, the convective pattern has spread over the entire cell and the rolls are clearly distinguishable not only in the liquid, but also in the gas phase. As ΔT is increased further, to 20 K, the convection in both layers becomes more vigorous. While convection has a progressively significant effect on the temperature in the liquid layer, the temperature field in the gas layer remains qualitatively similar for $\Delta T \leq 20$ K.

The wave length of the convective pattern appears to grow monotonically with ΔT. The number of convection rolls first increases, as the pattern expands from the hot to the cold wall, and after the multicellular pattern is established, the number of rolls steadily decreases, until the convection pattern becomes

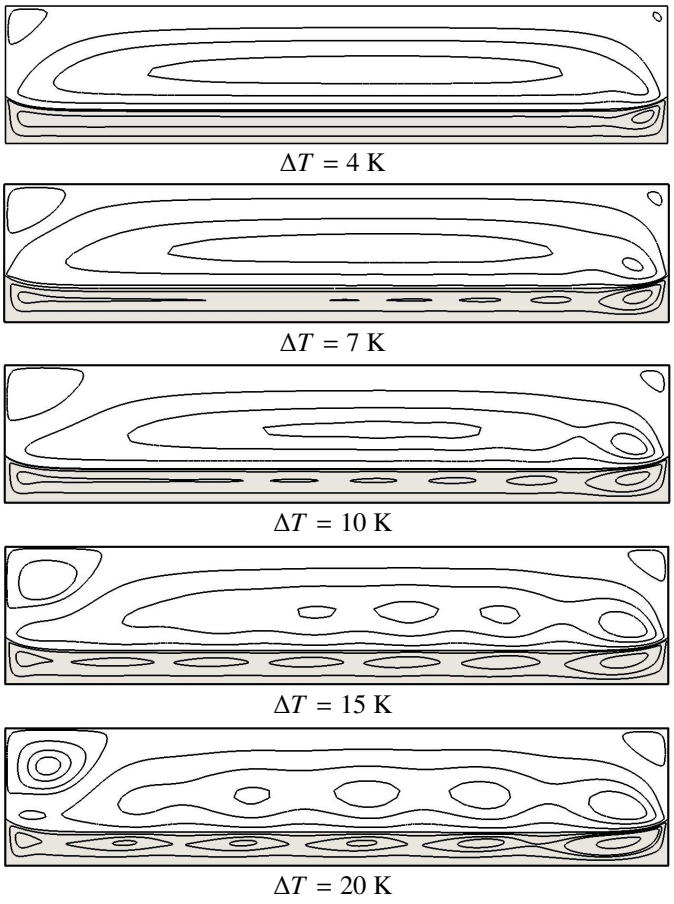

Figure 3: Dependence of the flow field on the imposed temperature difference ΔT. Solid lines represent the streamlines of the flow. Here and below, the gray (white) background indicates the liquid (gas) phase.

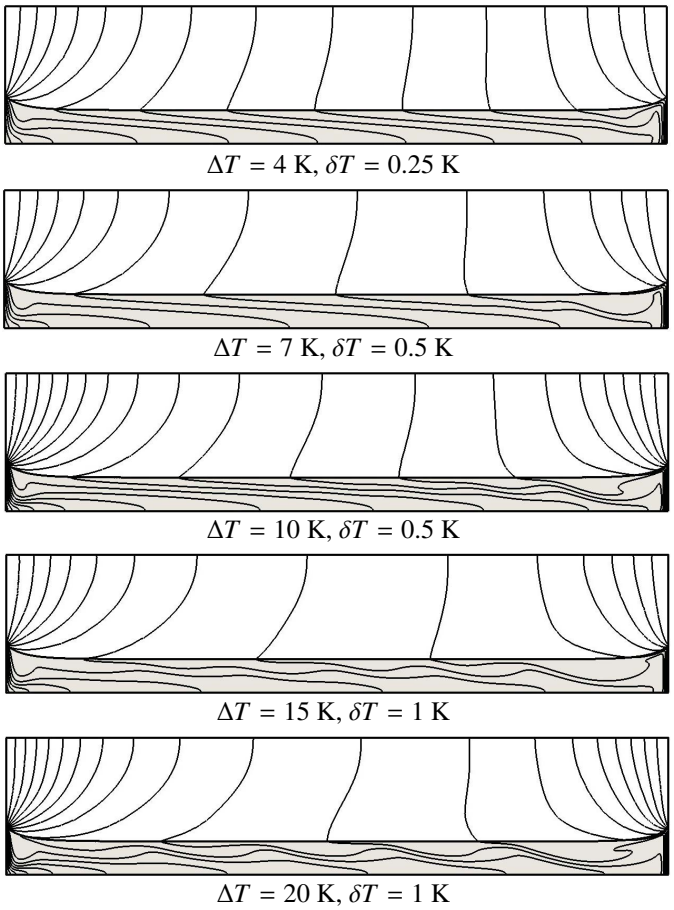

Figure 4: Dependence of the temperature field inside the cavity on the imposed temperature difference ΔT. Solid lines represent the isotherms, with temperature difference δT between them as indicated.

time-dependent at higher ΔT. This trend is consistent with both experiments of Riley and Neitzel [7] and the numerical simulations of Shevtsova *et al.* [17].

In order to directly compare our results with other numerical, experimental, and analytical studies, we need to determine the Marangoni number (29) based on the interfacial temperature gradient τ, which characterizes the magnitude of thermocapillary stresses. As it has been pointed out in numerous previous studies, τ differs rather significantly from the imposed gradient $\Delta T/L$. As a result, the interfacial Marangoni number (29) differs rather significantly from the "lab" Marangoni number

$$Ma_L = \frac{\gamma d_l^2 \Delta T}{\mu_l \alpha_l L} \tag{30}$$

used in the earlier studies and based on the applied temperature difference ΔT. While at lower ΔT the interfacial temperature (shown in Fig. 5) in the core region of the flow varies linearly with position x, for higher ΔT there is significant modulation due to convection in the liquid. Hence we chose to use a spatially averaged value of the gradient which corresponds to a linear fit to the graph of $T_i(x)$. For ΔT = 4, 7, 10, 15, and 20 K we find, respectively, Ma_l = 342, 460, 547, 682, and 804. In the range of ΔT where the flow is steady, $\Delta T/L$ is found to vary as a rational function of τ, as Fig. 6 shows. In the limit $\Delta T \to 0$ the fit correctly reproduces the analytical solution

$$\left.\frac{\Delta T}{L}\right|_{\Delta T \to 0} = \left(1 + 2\frac{k_l}{k_w}\frac{h_w}{L}\right)\tau = 1.00368\tau, \tag{31}$$

which corresponds to a conductive profile in the liquid layer.

At low values of Ma_l the unicellular flow in the core region of the test cell agrees with the analytical solution originally obtained by Kirdyashkin [8] and later corrected by Villers and Platten [9]. For the thermocapillarity-buoyancy driven flow in an extended layer subject to horizontal temperature gradient with adiabatic boundary conditions at the bottom and the free surface of the liquid layer, one finds that the horizontal component $u_{l,x}$ of the velocity and temperature T_l can be written in dimensionless form as

$$\bar{u}_{l,x} = -Re_l\left[\frac{3\bar{z}_l^2}{4} - \frac{\bar{z}_l}{2} - Bo_l\left(\frac{\bar{z}_l^3}{6} - \frac{5\bar{z}_l^2}{16} + \frac{\bar{z}_l}{8}\right)\right], \tag{32}$$

and

$$\bar{T}_l = \bar{x}_l + Ma_l\left[\frac{\bar{z}_l^3}{12} - \frac{\bar{z}_l^4}{16} + Bo_l\left(\frac{\bar{z}_l^5}{120} - \frac{5\bar{z}_l^4}{192} + \frac{\bar{z}_l^3}{48}\right)\right], \tag{33}$$

where $\bar{u}_{l,x} = u_{l,x}d_l/\nu_l$, $\bar{T}_l = T_l/\tau d_l$, $\bar{x}_l = x/d_l$, $\bar{z}_l = z/d_l$, and $z = 0$ at the bottom of the liquid layer. It should be emphasized

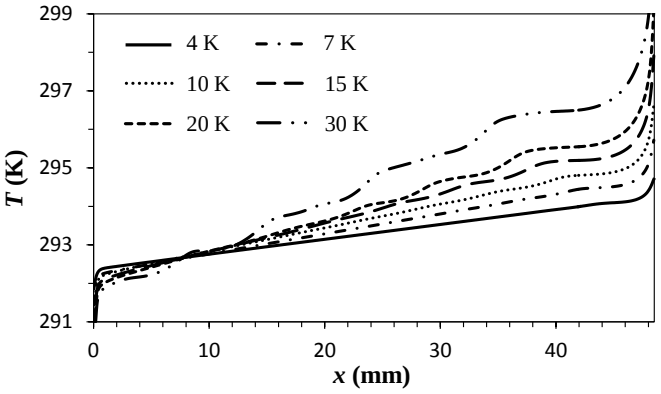

Figure 5: Interfacial temperature for different imposed temperature difference ΔT. The y-axis is truncated so that the details of the temperature variation in the core region of the flow can be seen.

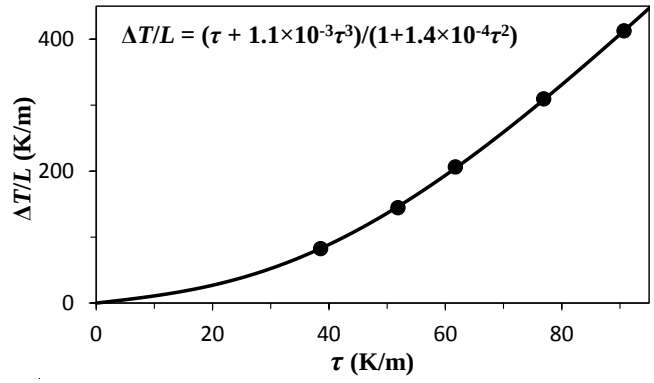

Figure 6: The relation between the gradient τ of the interfacial temperature in the core region of the flow and the imposed temperature gradient $\Delta T/L$. For steady flows (ΔT = 4, 7, 10, 15, 20 K) the dependence can be fitted with extremely high accuracy (R^2 = 0.9999) by a low order rational function.

that solutions (32) and (33) are only valid if we assume that $\partial T_i/\partial x = \tau$ = const. This assumption *does not* follow from the proper boundary conditions for the two-sided problem at the free surface (and, in fact, breaks down for higher ΔT, as Fig. 5 illustrates), and hence has to be checked for consistency. Before we perform this consistency check, however, let us compare these analytical solutions with numerical ones for lower values of ΔT, where this assumption appears to hold.

As Fig. 7 illustrates, we find excellent agreement, for both the velocity and temperature profile, in the middle of the test cell for moderate temperature differences ΔT = 4 K and ΔT = 7 K at which unicellular flow is found. The computed flow velocity is also in reasonably good agreement with experimental measurements (despite the slight difference in the applied ΔT and the numerics being restricted to 2D). We find the maximum and minimal values of $u_{l,x}$ are $u_{\min} = -3.6$ mm/s and $u_{\max} = 1.2$ mm/s for ΔT = 4 K and d = 2.45 mm (which corresponds to Ma_l = 342.3 and Bo_l = 0.85), while experimental observations [28] give $u_{\min} = -3.7$ mm/s and $u_{\max} = 1.3$ mm/s for ΔT = 3.8 K and d_l = 2.5 mm (which corresponds to Ma_l = 370 and Bo_l = 0.89).

The assumption that the interfacial temperature varies lin-

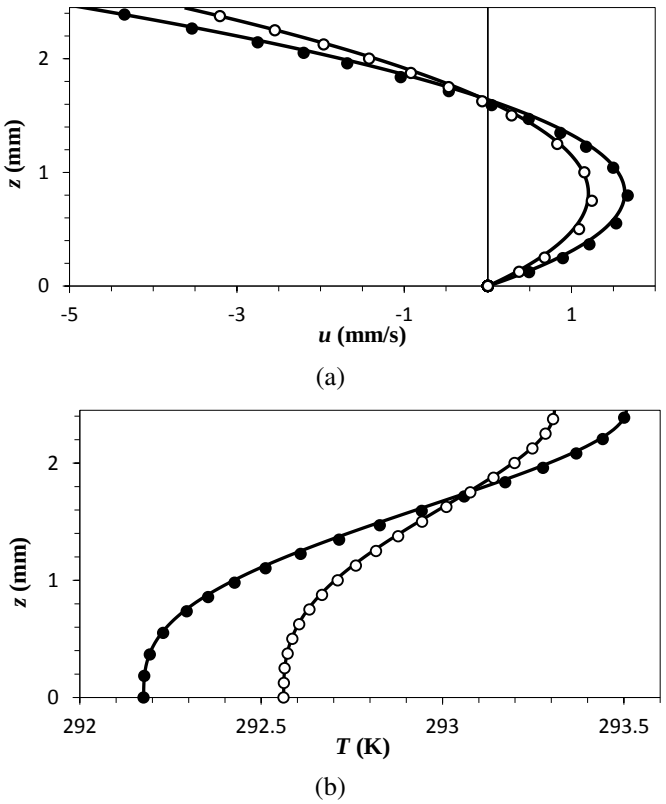

Figure 7: Vertical profiles of the horizontal velocity $u_{l,x}$ (a) and temperature T_l (b) in the liquid layer in the middle of the cell, $x = L/2$. Open and close circles correspond to numerical results for ΔT = 4 K and ΔT = 7 K, respectively; solid lines show the theoretical predictions.

early in the core region of the flow has been widely used in previous studies, without much justification, both for deriving the expressions (32) and (33) for the return flow underlying the stability analyses [10, 11, 13] as well as in models of the adiabatic section of heat pipes [29, 30, 31], which assume unidirectional flow in the liquid phase. However, the validity of this assumption cannot be established by a one-sided model which ignores the transport in the gas phase. Proper justification requires showing that this assumption is consistent with a steady-state solution of the transport equations in the gas phase which satisfies all of the boundary conditions at the free surface.

We can find the solutions for the gas velocity $v_{g,x}$ and vapor density ρ_v in the core region in the same way the solutions (32) and (33) where obtained in the liquid phase. Solving (1) subject to the continuity of the velocity at the interface $z = d_l$ and the no-slip boundary condition at the top wall $z = H$ of the cell yields

$$\bar{u}_{g,x} = -\mathcal{R}\left[\frac{3\bar{z}_g^2}{4} - \frac{\bar{z}_g}{2} - \mathcal{B}\left(\frac{\bar{z}_g^3}{6} - \frac{5\bar{z}_g^2}{16} + \frac{\bar{z}_g}{8}\right)\right], \tag{34}$$

while solving (6) subject to the no-flux boundary conditions at the top and bottom of the gas layer we find

$$\bar{\rho}_v = \bar{x}_g + \frac{\nu_g}{D}\mathcal{R}\left[\frac{\bar{z}_g^3}{12} - \frac{\bar{z}_g^4}{16} + \mathcal{B}\left(\frac{\bar{z}_g^5}{120} - \frac{5\bar{z}_g^4}{192} + \frac{\bar{z}_g^3}{48}\right)\right], \tag{35}$$

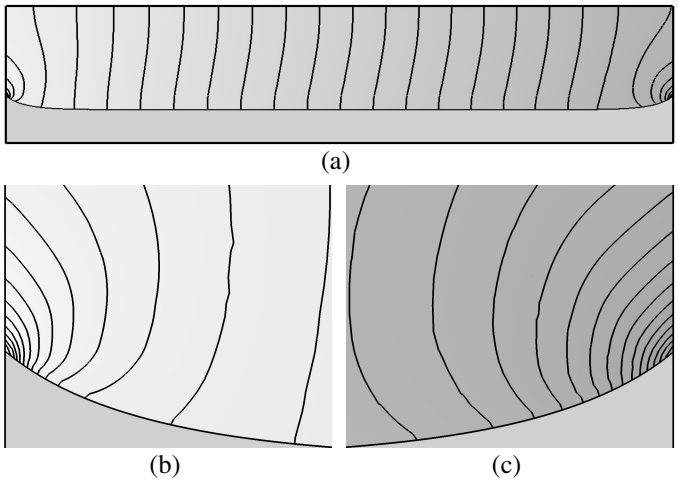

Figure 8: Vapor concentration c_v in the gas phase for $\Delta T = 4$ K. Entire cell (a) and the blow-ups of the 3 mm-wide regions near the contact line at the cold end wall (b) and near the contact line at the hot end wall (c). The difference between adjacent level sets is $\delta c = 0.02\%$ in (a) and $\delta c = 0.01\%$ in (b) and (c). Darker shade indicates higher concentration, ranging from 3.82% to 4.46% in the gas phase. The concentration field is not defined in the liquid phase.

where $\bar{u}_{g,x} = u_{g,x} d_g/\nu_g$, $\bar{\rho}_v = \rho_v/\varrho d_g$, $\bar{x}_g = x/d_g$, $\bar{z}_g = (H - z)/d_g$, $d_g = H - d_l$ is the thickness of the gas layer, and ϱ is some constant. Finally, the parameters $\mathcal{R}$ and $\mathcal{B}$ incorporate the properties of both fluid layers,

$$\mathcal{R} = \frac{\nu_l d_g}{\nu_g d_l} Re_l + \frac{1}{12}\left[\frac{\nu_l d_g}{\nu_g d_l} Gr_l + Gr_g\right],$$
$$\mathcal{B} = -\frac{Gr_g}{\mathcal{R}}, \tag{36}$$

where the Grashof number in the gas layer is defined using the formula analogous to that for the liquid layer. Note that $\mathcal{B}$ is negative, that is buoyancy forces recirculation of the gas in the direction opposite to that of thermocapillarity, as illustrated by the flow fields shown in Fig. 3.

Since both T_v and p_g are essentially constant (the variation in T_v over the core region of the flow is about 0.4% for $\Delta T = 4$ K, while the pressure drop due to viscous effects is negligible compared with ambient pressure), the concentration field is essentially proportional to the vapor density, so that (35) yields:

$$c_v = \frac{\bar{R}_v T_v}{p_g}\rho_v \approx \frac{\bar{R}_v T_0}{p_g}\varrho(x - x_0) + h(z), \tag{37}$$

where x_0 is some point in the core region of the flow and $h(z)$ is some function of z defined by the second term in (35). Indeed, the numerical solution shown in Fig. 8(a) has precisely this form in the core region of the flow, where J is negligibly small and the no-flux boundary condition for ρ_v is justified.

It should be pointed out that there is no solution analogous to (33) for T_g. Although the velocity profiles (32) and (34) are similar and the temperature is governed by an advection-diffusion equation (11) in both phases, the boundary conditions for T_g are not symmetric: we have an adiabatic boundary condition at the top of the cavity, but at the free surface we have instead the continuity condition $T_g = T_i = T_l$. As a result, (11) does not admit a solution in the form such as (33). Indeed, the numerical solutions shown in Fig. 4 illustrate that the temperature field in the gas layer has a considerably more complicated shape.

Having obtained the solution for the vapor concentration, we can proceed to compute the saturation temperature T_s at the interface, which is a function of c_v via (10) and (15):

$$T_s(x) \approx T_s(x_0) + \left[\frac{\partial T_s}{\partial p_v}\frac{\partial p_v}{\partial c_v}\frac{\partial c_v}{\partial x}\right]_{x_0}(x - x_0). \tag{38}$$

Since both $\partial p_v/\partial c_v = p_g$ and $\partial c_v/\partial x$ are independent of x, if c_v does not vary significantly across the cell (so that $\partial T_s/\partial p_v$ can also be considered constant), we find T_s to vary linearly in x.

Finally, the interfacial temperature T_i can be obtained from (13). The pressure jump across the interface (the Young-Laplace pressure) is small for curvatures corresponding to the capillary length, so the first term in (13) is negligible compared to the second one. Dropping it and solving for T_i we find

$$\frac{T_i - T_s}{T_s} \approx \frac{2 - \lambda}{2\lambda}\frac{\bar{R}_v T_s}{\mathcal{L}}\sqrt{\frac{2\pi}{\bar{R}_v T_s}}\frac{J}{\rho_v}. \tag{39}$$

where the right-hand-side is much smaller than unity (for $\Delta T = 10$ K, the typical values are of order 10^{-7} in the core region and of order 10^{-5} near the end walls) due to the relatively large values of the latent heat. This means that T_i is essentially identical to T_s at the interface. Combining (38), (37), and (15) we find

$$\tau \approx \frac{\partial T_s}{\partial p_v}\frac{\partial c_v}{\partial x}p_g \approx \frac{\bar{R}_v^2 T_0^3}{\mathcal{L}}\varrho. \tag{40}$$

Hence, the interfacial temperature gradient is constant in the core region of the flow and set by the gradient of the vapor concentration in the gas phase. However, the temperature will deviate from a linear profile if either c_v changes significantly (e.g., when the gas phase is dominated by vapor, rather than air) or the adiabatic boundary condition on the liquid side of the interface breaks down (e.g., as a result of convection at higher ΔT).

Near the end walls the assumptions and approximations valid in the core region break down anyway and we can no longer expect a linear dependence of T_i on x. Indeed, as Fig. 5 shows, the interfacial temperature changes very quickly near the end walls. In fact, the corresponding thermal boundary layers account for a significant fraction of the imposed temperature difference ΔT. The remainder of the temperature drop takes place inside the end walls, as can be seen in Fig. 9. In the present setup the variation in T_i over the core region of the flow (roughly τL), the temperature drop across the thermal boundary layers and that inside the end walls (in the regions wetted by the liquid), are all comparable.

As shown in Fig. 9, the inner side wall temperature varies significantly with height, reflecting the variation in the temperature drop across the walls. This temperature drop is negligible where the wall is in contact with the gas for which $k_w \gg k_g$, but quite large below the contact line, since k_w is comparable to k_l. The largest temperature drop is at the contact line, where heat

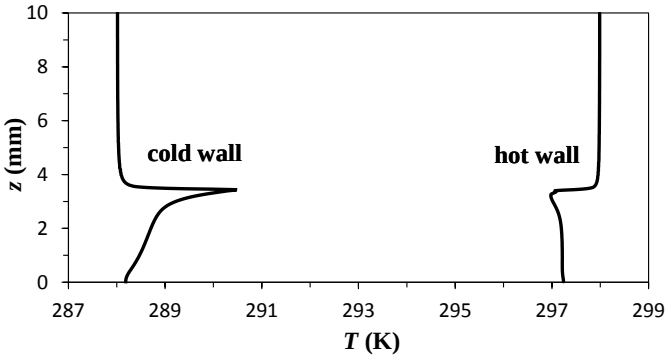

Figure 9: Temperature distribution along the inner surfaces of the end walls. The temperature imposed on the outer surfaces of the cold and hot walls are $T_c = 288$ K and $T_h = 298$ K, respectively, which corresponds to $\Delta T = 10$ K.

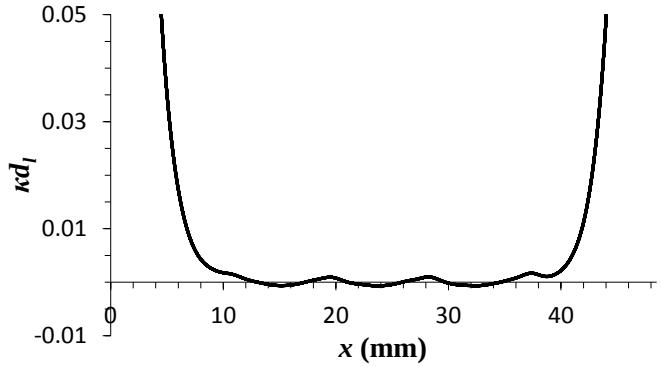

Figure 10: Nondimensional curvature of the liquid-vapor interface for $\Delta T = 20$ K. The variation in the sign reflects the distortion of the interface due to strong convection in the liquid layer. The vertical range has been truncated to amplify the variation in the core region of the flow.

conduction through the wall is balanced not only by the heat conduction through the liquid, but also by the heat released or absorbed as a result of phase change at the interface. It should be pointed out, however, that the there is also a strong asymmetry between the two end walls: the temperature drop below the contact line is relatively uniform along the hot wall, but varies by an order of magnitude (between 0.2 K and 2.5 K) along the cold end wall.

The detailed model which describes heat and mass transport in both the liquid and the gas phase can also be used to validate the boundary conditions used in the one-side models. In particular, the interface is assumed to be flat in the core region. Fig. 10 shows the curvature κ of the interface, which has been nondimensionalized by the thickness d_l of the liquid layer. The relatively high curvature near the end walls is caused by the distortion of the interface due to the low contact angle. At this higher temperature difference ($\Delta T = 20$K), the interface in the core region of the flow is not perfectly flat: the sign of the curvature oscillates, indicating a stationary surface wave caused by the convection rolls in the liquid layer. However, the amplitude of these oscillations is quite small (and becomes even smaller for smaller ΔT), so the interface can be considered essentially flat (and rigid) in the core region (roughly 10 mm $\lesssim x \lesssim$ 40 mm).

Existing one-sided models also ignore phase change at the interface, which is justified for liquids with low vapor pressures, such as decane, but certainly not for volatile liquids, such as acetone or low viscosity silicone oils. In order to determine whether phase change can indeed be ignored, we have defined a nondimensional mass flux $\bar{J} = J/J_0$, where J_0 is the mass flux *along* the interface due to the flow in the liquid layer,

$$J_0 = \rho_l u_i. \tag{41}$$

Here u_i is the tangential component of the velocity at the interface, which can be computed using the analytical solution (32). As shown in Fig. 11, for the volatile silicone oil considered in this paper, the phase change is localized to the boundary layers near the end walls. More importantly, in the core region of the flow mass flux across the interface due to phase change is indeed negligibly small compared to J_0.

Most one-sided models use Newton's law of cooling

$$\mathbf{n} \cdot \nabla T_l = Bi\,(T_0 - T_i), \tag{42}$$

where Bi is the Biot number, instead of the proper heat flux balance (19). For the adiabatic boundary condition at the bottom of the liquid layer, the analytical solution such as (33) is only valid if the *normal* component of the heat flux $q_l = k_l \mathbf{n} \cdot \nabla T_l$ in the liquid at the interface also vanishes, which corresponds to the limit $Bi = 0$. We can check whether q_l is vanishingly small by defining a nondimensional heat flux $\bar{q}_l = q_l/q_0$, where q_0 is the conductive heat flux through the liquid layer along the z direction,

$$q_0 = k_l \frac{\delta T}{d_l}, \tag{43}$$

and δT is the temperature difference across the liquid layer (e.g., $\delta T = 0.75$ K for $\Delta T = 4$ K). Again, Fig. 11 shows that q_l is small compared to q_0 in the core region of the flow (3% or less), mostly justifying the use of the adiabatic boundary condition at the interface away from the end walls. Moreover, we see a high degree of correlation between $\bar{J}$ and $\bar{q}_l$. Indeed, this is to be expected, since by ignoring the heat conduction in the gas phase we can reduce (19) to $q_l = \mathcal{L}J$. However, there are regions near the end walls where the heat flux $q_g = k_g \mathbf{n} \cdot \nabla T_g$ in the gas phase cannot be ignored, as is typically done in one-sided models.

Furthermore, a closer inspection of Fig. 11 shows a rather counter-intuitive result. There is a region near the cold wall (0.1 mm $< x <$ 1.8 mm) where the liquid evaporates ($J > 0$), and another region near the hot wall (45 mm $< x <$ 48.1 mm) where the vapor condenses ($J < 0$). Everywhere else the sign of J is as one would expect. For instance, vapor condenses immediately next to the cold wall (0 mm $< x <$ 0.1 mm) and liquid evaporates immediately next to the hot wall (48.1 mm $< x <$ 48.5 mm). Our intuition, however, is shaped primarily by cases involving thin films, where heat is transported through the liquid diffusively: when the wall temperature is higher (lower) than the local saturation temperature T_s, so is the interfacial temperature T_i, and we expect evaporation (condensation). In this

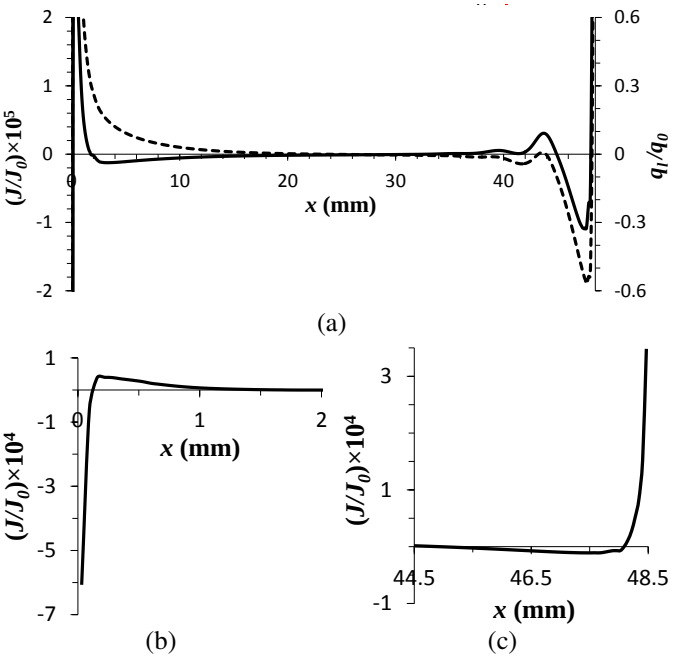

Figure 11: Nondimensional mass flux $\bar{J}$ (solid line) and nondimensional heat flux $\bar{q}_l$ in the liquid towards the interface (dashed line) for unicellular flow, $\Delta T = 4$ K. In (a) the vertical range has been truncated to amplify the variation in the core region of the flow. Panels (b) and (c) show the variation of the mass flux over its entire range near the end walls.

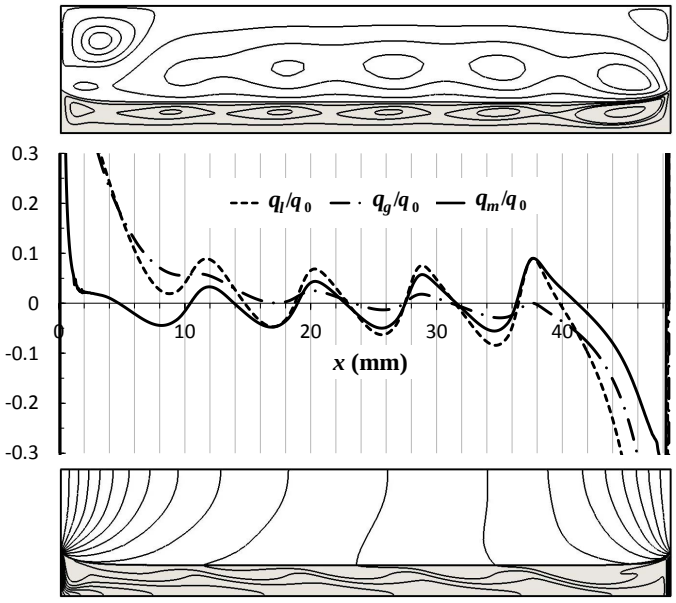

Figure 12: Flow structure, heat flux, and temperature field for the case when $\Delta T = 20$ K. The middle panel shows the (nondimensionalized) conductive heat flux at the liquid side $q_l = \mathbf{n} \cdot k_l \nabla T_l$, the vapor side $q_g = \mathbf{n} \cdot k_g \nabla T_g$, and the heat flux associated with phase change, $q_m = \mathcal{L}J = q_l - q_g$. The vertical range has been truncated to amplify the variation in the core region of the flow.

particular geometry, we expect condensation near a cold wall (where the wall temperature is lower than T_s) and evaporation near a hot wall (where the wall temperature is higher than T_s). Indeed, this is what we find very close to the end walls (within 0.1-0.4 mm). A little further away, heat transport is dominated by advection, not diffusion (as the shape of the isotherms in Fig. 4 clearly illustrates), and T_i can easily become higher (lower) than T_s near a cold (hot) wall. As it turns out, this is exactly what happens.

As we already mentioned, there is a high degree of correlation between J and q_l, so it is natural to expect that it is the heat flux in the liquid (towards or away from the interface, depending on the local flow field) that controls the sign of J. In order to see how the flow in the liquid affects the phase change at the interface, it is instructive to compare the flow field, the temperature field, the normal heat flux, and the mass flux for the case $\Delta T = 20$ K featuring multiple convection rolls. As Fig. 12 shows, in the presence of convection rolls neither the heat fluxes at the two sides of the interface nor the mass flux (which is proportional to the latent heat associated with phase change, $\mathcal{L}J = q_m = q_l - q_g$) are negligible in the core region of the flow. Both J and q_l are modulated by convection in the liquid, with the minima of J and q_l located above the rolls and the maxima located between the rolls, while the heat flux q_g in the gas phase is considerably smaller (although still non-negligible). In particular, we find that q_l can be as high as 10% of q_0 and q_g as high as 5% of q_0 in the core region of the flow, illustrating the breakdown of the adiabatic boundary condition in the multicellular regime.

The same relation applies to the rolls adjacent to the end walls. In particular, we find a region of condensation above, and a narrow region of evaporation to the right of, the roll adjacent to the hot end wall for both $\Delta T = 20$ K and $\Delta T = 4$ K. The roll adjacent to the cold end wall is too weak to drive condensation right above it. However, the flow near the stagnation point at the contact line is fast enough at all ΔT to invert the sign of q_l and cause evaporation in a narrow region close to the cold wall. Right at the contact line the velocity vanishes and q_l becomes negative, producing an even narrower region of condensation.

3.2. Time-Periodic Multicellular Flow

As ΔT is increased beyond 20 K, the stationary convection pattern becomes unstable and the flow becomes unsteady. In particular, for $\Delta T = 30$ K (which corresponds to $Ma_l \approx 1096$), the flow is time-periodic, with period $T \approx 3.2$ s. Fig. 13 shows the stream function ψ in the liquid layer at different times during one period. Just as for the stationary convection at lower ΔT we find multiple convection rolls. However, the regularity in the strength and position characteristic of stationary patterns is lost in the time-periodic case.

Riley and Neitzel [7] refer to this flow as oscillatory multicell (OMC). Our results suggest that this term may not be completely accurate. The flow near the hot wall is indeed oscillatory. The roll adjacent to the hot(right) wall (labeled A in Fig. 13) has both a larger size and greater strength than other rolls. Starting from the time $t = 0$, roll A grows, mostly in the x direction during the first half of the period. As it is elongated, a new roll (labeled B) forms at the left edge of roll A around $t = (3/8)T$. During the second half of the period, roll A starts to shrink, and the new roll B is "pinched" off around $t = (5/8)T$, and recedes from roll A. The strength or roll B gradually decreases and it then travels back towards roll A, merging with A

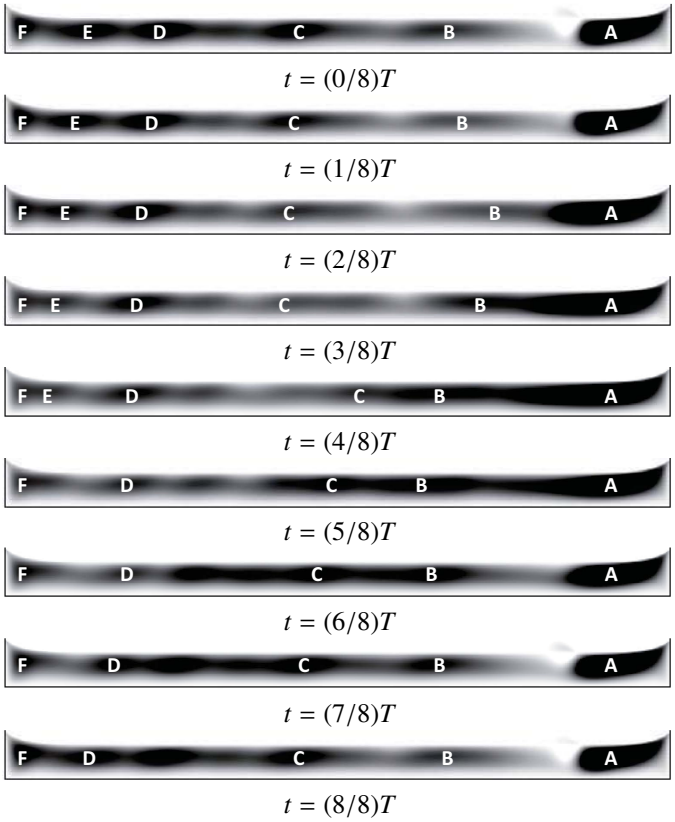

Figure 13: Stream function in the liquid layer at different times during one period of oscillation for $\Delta T = 30$ K. The shaded background represents the value of the stream function ψ, with darker color indicating higher values of ψ. The time interval between consecutive images is approximately 0.4 s. High-resolution movie showing the evolution of the flow field and the temperature field can be downloaded *here*. The movie shows five periods (which corresponds to about 16.4 s). The upper panel shows the temperature T, the middle panel – the stream function ψ, and the lower panel – the magnitude of the velocity $\mathbf{u}$. The standard jet color map is used with blue corresponding to the minima and red – the maxima. The range of variation for T is 289 to 297 K and for $|\mathbf{u}|$ is 0 to 15 mm/s.

around $t = (2/8)T$. This is quite similar to what the numerical simulations of Villers and Platten [4] showed for a liquid layer with a streamwise aspect ratio substantially smaller than that studied here ($\Gamma_x = 9$, vs. $\Gamma_x = 18.6$).

Near the cold end, the dynamics are best described as a traveling wave. We find several convection rolls, two of which are labeled D and E in Fig. 13, traveling to the left. Both rolls D and E keep moving towards the stationary roll F adjacent to the cold wall. Around $t = (3/8)T$ roll E starts to merge with roll F, disappearing around $t = (5/8)T$. Roll D keeps traveling to the left, taking at $t = (8/8)T$ the position of roll E at $t = (0/8)T$, after which the process repeats. It should be noted that both the strength of the rolls and the speed at which they travel towards the cold wall varies considerably.

In the middle of the cell, it is harder to distinguish individual convection rolls. The dynamics are dominated by a roll (labeled C) which nucleates at the right edge of the central region around $t = (4/8)T$, just to the left of roll B, travels to the left edge of the central region and disappears there around $t = (3/8)T$. Summing up, we find that the time-periodic flow is

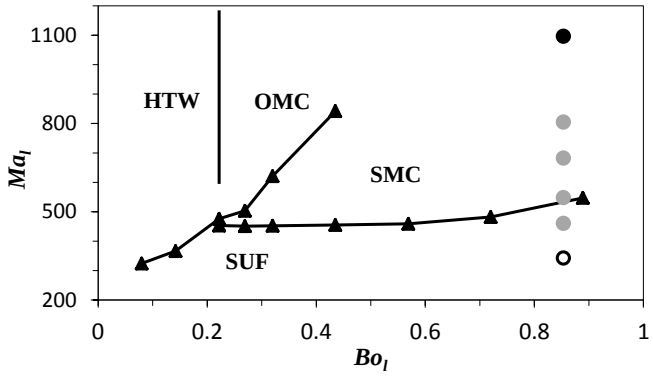

Figure 14: The flow regimes observed for different Bo_l and Ma_l. The lines show transitions between different flow regimes in the experiments of Riley and Neitzel [7]. The labels denote steady unicellular flow (SUF), steady multicellular flow (SMC), oscillating multicellular flow (OMC) and hydrothermal waves (HTW). Open squares correspond to Ma_L and closed squares – to Ma_L. The circles show the results of our simulations. White fill denotes steady unicellular flow, gray – steady multicellular flow, and black – oscillating multicellular flow.

rather complicated, with oscillatory dynamics near the hot end wall, a traveling wave near the cold end wall, and dynamics in the middle which appear to be some sort of mixture of the regimes found near the two end walls.

The flow behavior found in the numerics is qualitatively consistent with the experimental observations of Li *et al.* [28]. Their experiments also show oscillatory dynamics on one side of the cavity (periodic modulation of the width of the roll nearest the hot wall) and traveling motions on the opposite side (rolls traveling towards the cold end wall).

3.3. Comparison with Experiment

This section summarizes our numerical results and compares them with experimental results in relevant geometries. The comparison has a qualitative nature as certain aspects of the experimental flow cells differ from the 2D simulations presented here. In most studies the flow cell is not sealed and the liquid is in direct contact with the temperature-controlled end walls, while our simulations assume that the fluid is contained in a sealed thin-walled container (see Fig. 1). Furthermore, the variation in the contact angle leads to slight variation in the thickness of the liquid layer and the slope of the free surface near the walls, which affect the strength of both the buoyancy force and the thermocapillary stresses.

The experiments performed by Riley and Neitzel [7] were in a geometry (a cavity with a flow section of length $L = 50$ mm and width $W = 30$ mm), which is the closest to that used in our 2D numerical simulations. For the range of liquid depths considered ($0.75 \text{ mm} \le d_l \le 2.5$ mm) these parameters correspond to the streamwise and spanwise aspect ratios of $12 \le \Gamma_x \le 40$ and $20 \le \Gamma_y \le 66.7$ (compared with $\Gamma_x = 18.6$ and $\Gamma_y = \infty$ used here). The working fluid in the experiment was 1 cS Dow Corning silicone oil with $Pr_l = 13.9$, while we used a substantially more volatile silicone oil with $Pr_l = 6.8$.

Fig. 14 (adapted from Ref. [7]) compares the flow regimes observed in experiment with those found in our simulations. In

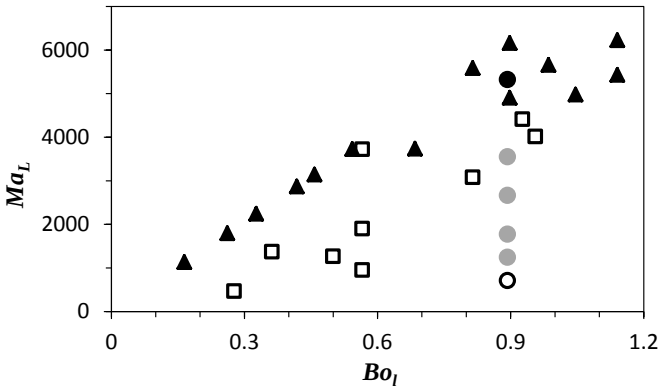

Figure 15: The flow regimes observed for different Bo_l and Ma_L. Filled triangles and open squares represent, respectively, oscillatory and stationary flow patterns observed by Villers and Platten [4]. The circles show the results of simulation, with notations as in Fig. 14.

the numerics the dynamic Bond number $Bo_l = 0.853$ is constant since the fluid thickness does not vary. As ΔT increases, the interfacial Marangoni number increases, and the flow pattern is found to transition from steady unicellular flow to steady multicellular flow, then to oscillating multicellular flow. In particular, in the numerics the transition from SUF to SMC occurs at $342 < Ma_i < 460$, which is below the critical value $Ma_i \approx 540$ extrapolated from the experimental data (Riley and Neitzel determine the transition threshold between OMC and SMC based on the splitting of the convection roll closest to the hot wall). This is consistent with the general trend of the critical Ma_i increasing with Pr (for $Pr \gtrsim 1$) [13]. The transition from SMC to OMC takes place for $804 < Ma_i < 1096$ in the numerics. Unfortunately, Riley and Neitzel do not report the critical Ma_i for the transition to OMC for $Bo_l > 0.5$.

Another useful reference is provided by the experiments of Villers and Platten [4] which used a cavity with a flow section of length $L = 30$ mm and width $W = 10$ mm and a liquid layer thickness $1.70 \text{ mm} \le d_l \le 14.25$ mm, corresponding to $2.1 \le \Gamma_x \le 17.6$ and $0.7 \le \Gamma_y \le 5.9$. The working fluid was acetone with $Pr_l = 4.2$. The experimental observations are only classified as either stationary or oscillatory flow, so we can only compare the critical Marangoni number for transition from SMC to OMC. Villers and Platten only quote the laboratory Marangoni number (30), so we use the (Bo_l, Ma_L) plane to present the results. As Fig. 15 shows, the transition to OMC occurs at comparable values of Ma_L in the experiment and in the numerics, although, again, quantitative agreement is not expected due to the difference in the values of Pr and strong lateral confinement present in the experiment.

The experiments of Li *et al.* [28] match the numerical simulations presented here almost exactly (same fluid, same length and height of the cavity). However, there is a discrepancy in the critical Marangoni numbers characterizing different transitions. In the experiment the transition from SUF to SMC happens at $Ma_l \approx 240$ and the transition from SMC to OMC at $560 < Ma_l < 610$, with both values lower than our numerical predictions by about 30%. Furthermore, for the oscillatory flow, the dynamics of convection rolls in the experiment are very similar to our numerical results. The temporal period in the experiment is larger ($T = 5.4$ s) than in the numerics ($T = 3.2$ s), which is not surprising given that the experimental flow corresponds to a lower value of Ma_i.

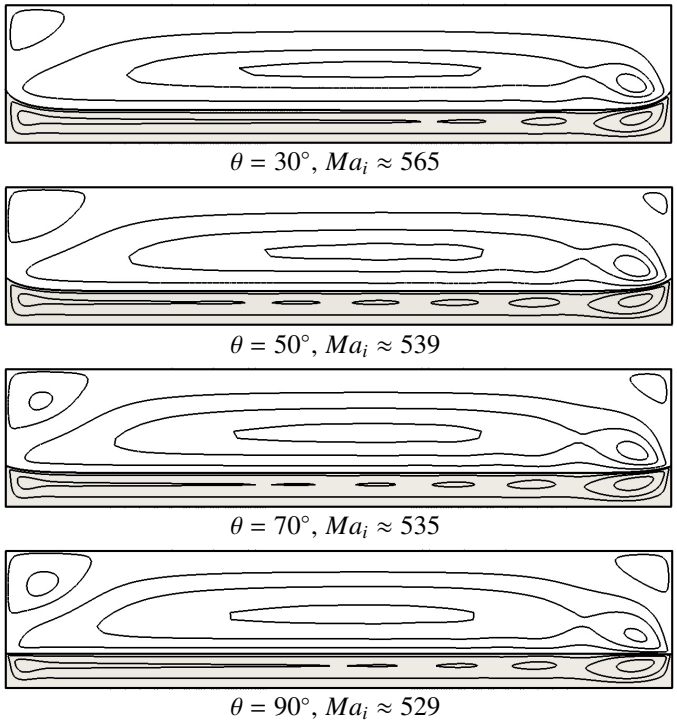

Figure 16: Streamlines of the steady flow for different values of the contact angle θ. $\Delta T = 10$ K and the average thickness of the liquid layer is $d_l \approx 2.5$ mm.

The discrepancies in the critical Ma_i may be due to a number of reasons. Lateral confinement effects are one example. The finite width $W = 10$ mm of the experimental cell used in Ref. [28] (which corresponds to Γ_y of only 4.1) causes a curvature of the free surface in the spanwise direction and a deviation in the layer thickness at the side walls from the transversely flat profile assumed by the numerical simulations. The experiments also show evidence of weak secondary flow in the (y, z) plane which is not present in the numerics and could modify the temperature distribution in the liquid layer. In order to investigate the effects of the contact angle and three-dimensionality of the flow we performed additional studies described below.

3.4. The Effect of the Contact Angle

To investigate how the variation in the contact angle affects the flow we performed a series of 2D numerical simulations varying θ over a rather wide range. The geometry of the 2D cavity was kept the same as in previous simulations to facilitate comparison. The temperature difference between the outer surfaces of the two end walls was chosen to be $\Delta T = 10$ K for all the cases. This value is reasonably close to the transition from SUF to SMC, making the structure of the flow quite sensitive to the variation of any parameters.

The flow is found to depend on the value of θ, even in the core region away from the end walls, although this dependence is not very strong. For the four values of the contact angle that have been investigated, the flow patterns shown in Fig. 16 are qualitatively similar, although the values of Ma_i are slightly different (due to the change in the thickness of the liquid layer with θ). In the liquid layer, several weak convection rolls can be seen in the core region of the flow. We find four rolls for $\theta = 50^\circ$ and 70°, three for $\theta = 90^\circ$ and two for $\theta = 30^\circ$. In the gas layer, the flow patterns are almost indistinguishable. The temperature field (not shown), is essentially the same in the range of θ considered. Summing up, these results suggest that the influence of the contact angle on the flow pattern, both near the end walls and in the core region of the flow, is relatively weak and can only partially account for the disagreement between the experiment and numerics.

3.5. Three-Dimensional Effects

The effect of the lateral walls (lateral confinement for finite values of Γ_y) can only be understood by performing a full 3D simulation. However, simulating the flow in a cell of dimensions 48.5 mm × 10 mm × 10 mm used in Ref. [28] proved too time-consuming. The requirement to resolve the convective structures, despite the adaptively refined mesh, produces more than 10^6 computational cells (for 1/8 mm resolution). Matching the resolution of the 2D simulations (1/16 mm) would have required over 10^7 computational cells. Therefore, we chose to compare the results of 2D and 3D simulations for a cavity with inner dimensions of 15 mm × 5 mm × 5 mm ($L \times H \times W$), which has the additional benefit of enhancing the confinement effects. The thickness of the liquid layer was set to $d_l = 1.5$ mm, which corresponds to $Bo_l = 0.322$. Furthermore, to avoid confusing the effects of lateral confinement with the effects of the contact angle, we set $\theta = 90^\circ$ which produces an essentially flat free surface.

We have considered two different values of ΔT which place the system either in the unicellular or the multicellular steady flow regime. In particular, for $\Delta T = 4$ K (which corresponds to $Ma_l = 298$), we find a steady unicellular flow. Fig. 17 shows this flow in the vertical mid-plane of the 3D cavity which is almost indistinguishable from the corresponding 2D flow. Similarly, the temperature field in the mid-plane of the cavity is indistinguishable from the 2D solution (see Fig. 18).

In fact, both the flow field and the temperature field in 3D are very accurately represented by the 2D solution over most of the cavity interior. As Fig. 19 shows, the 3D and the 2D temperature field in the liquid are essentially identical at the horizontal plane at $z = 1$ mm passing the center of the two convection rolls. The vertical component of velocity u_z in the same horizontal plane is the same in 3D and in 2D (see Fig. 20) everywhere except near the side walls, where the 3D velocity vanishes due to no-slip boundary conditions.

For $\Delta T = 20$ K (which corresponds to $Ma_l = 602$), we find a steady multicellular flow. Fig. 21 shows that the flow in the vertical mid-plane of the 3D cavity, again, is almost indistinguishable from the corresponding 2D flow. The slight difference in the position of convection rolls is due to the weak

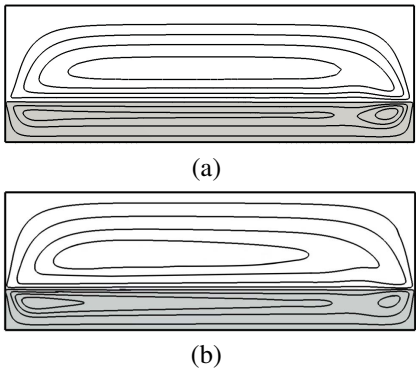

Figure 17: The flow in the vertical plane for $\Delta T = 4$ K. Streamlines of (a) the 2D flow and (b) the 3D flow in the mid-plane ($y = 2.5$ mm) of the cavity are shown.

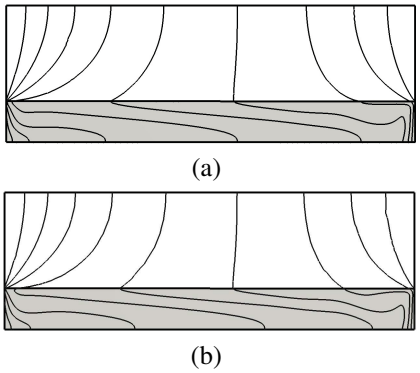

Figure 18: The temperature field in the vertical plane for $\Delta T = 4$ K. Isotherms of (a) the 2D solution and (b) the 3D solution in the mid-plane ($y = 2.5$ mm) of the cavity are shown. The temperature difference between two adjacent isotherms is $\delta T = 0.4$ K.

time-dependence of the 3D solution which slowly approaches a steady flow; the 3D flow structure becomes more similar to the 2D solution with time. Similarly, the temperature field in the mid-plane of the cavity is essentially indistinguishable from the 2D solution (see Fig. 22).

However, there are significant differences between the 3D and the 2D solution on either side of the vertical mid-plane, as the horizontal cross-section of the cavity illustrates. For instance, Fig. 23 shows that the strong modulation (in the x direction) of the 3D temperature field in the mid-plane disappears near the side walls, making the variation essentially monotonic. On the other hand, the vertical component of the 3D velocity field in the horizontal plane (see Fig. 24) shows that the convection rolls become strongly distorted. Instead of tilting, as linear stability analyses predict [10, 32], the rolls bend symmetrically, approaching the side walls at the same angle on both sides.

Summing up, we find that, for $\theta = 90^\circ$, 2D simulations provide a reasonably accurate description (both qualitative and quantitative) of the two-phase flow in the symmetry plane of the flow cell or cavity containing the fluid in a wide range of applied temperature gradients. For lower ΔT (in the SUF regime) the 2D solution is accurate everywhere except near the side walls. For higher ΔT (in the SMC regime) full 3D solution is required to describe the flow on either side of the symmetry plane. It is

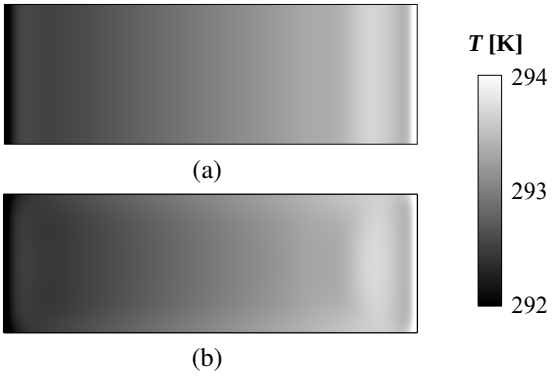

Figure 19: The temperature of the liquid in the horizontal plane $z = 1$ mm for $\Delta T = 4$ K. Shown are (a) the 2D solution and (b) the 3D solution.

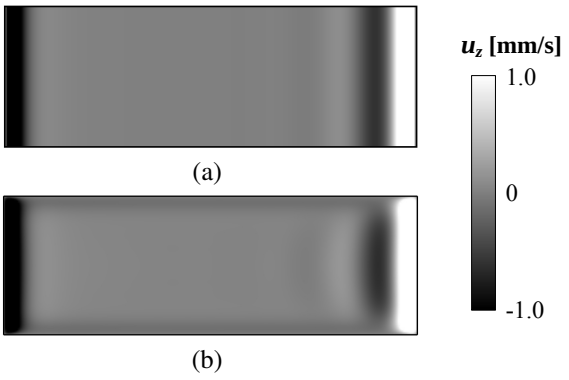

Figure 20: The velocity of the liquid in the horizontal plane $z = 1$ mm for $\Delta T = 4$ K. The vertical component u_z is shown for (a) the 2D solution and (b) the 3D solution.

possible that for small values of θ, which are more relevant for experiment, the variation of the thickness of the liquid film in the y direction could have a more pronounced effect on the flow structure and stability.

4. Conclusions

We have developed, implemented, and validated a comprehensive numerical model of two-phase flows of confined volatile fluids, which properly accounts for momentum, mass, and heat transport in both phases and phase change at the interface. This model was used to investigate the problem of buoyancy-thermocapillary convection in a sealed cavity subject to a horizontal temperature gradient, in the presence of air at atmospheric pressure, and was validated by comparing its predictions against known analytical solutions.

The numerical results were also compared with existing quantitative experimental data. We find good qualitative agreement for 2D simulations: as the Marangoni number is increased (while the dynamic Bond number is kept fixed), the flow undergoes transitions from steady unicellular to steady multicellular convection with co-rotating rolls, to time-periodic convection state. The critical values of the Marangoni number are similar to those found in experiment, but there are noticeable quantitative differences. To be fair, quantitative agreement was not

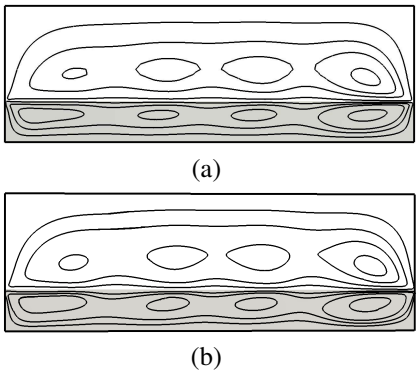

Figure 21: The flow in the vertical plane for $\Delta T = 20$ K. Streamlines of (a) the 2D flow and (b) the 3D flow in the mid-plane ($y = 2.5$ mm) of the cavity are shown.

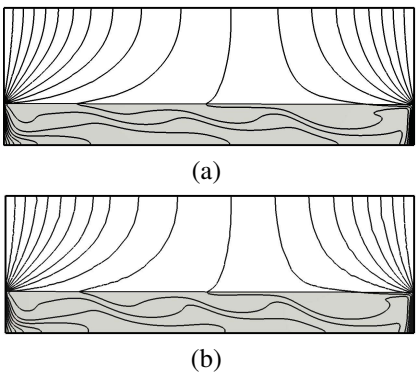

Figure 22: The temperature field in the vertical plane for $\Delta T = 20$ K. Isotherms of (a) the 2D solution and (b) the 3D solution in the mid-plane ($y = 2.5$ mm) of the cavity are shown. The temperature difference between two adjacent isotherms is $\delta T = 1$ K.

expected due to the differences between the numerical simulations and experiments (e.g., different Prandtl numbers of the working fluid and/or the geometry of the cavity).

We have attempted to investigate whether some of the differences could be due to geometric effects – specifically the curvature of the free surface due to wetting of the cavity walls by the fluid and the confinement effect of the side walls – but found that the convection pattern, at least in the symmetry plane of the cavity, is largely unaffected by these geometrical factors. Both the structure of the flow field and the temperature field were essentially the same in the 2D and the full 3D simulations, suggesting that, at least for liquid layers with a small to moderate transverse aspect ratio, 2D simulations provide reasonably accurate results.

The most likely reason for the discrepancies between the experiment and the numerics is the uncertainty in the values of various material parameters. Most notably, the value of γ reported in the literature ranges between 6.4×10^{-5} N/m-K [33], 8×10^{-5} N/m-K [34, 35] and 8.9×10^{-5} N/m-K [36, 37]. This is a variation of more than 30%, which changes both Ma and Bo_l by the same amount.

Numerical results, in turn, were used to validate the assumptions (of flat interface, negligible phase change, and negligible

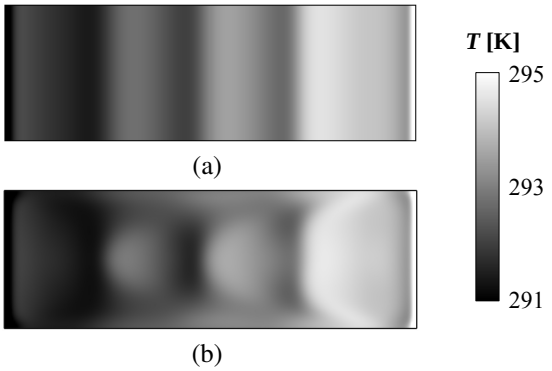

Figure 23: The temperature of the liquid in the horizontal plane $z = 1$ mm for $\Delta T = 20$ K. Shown are (a) the 2D solution and (b) the 3D solution.

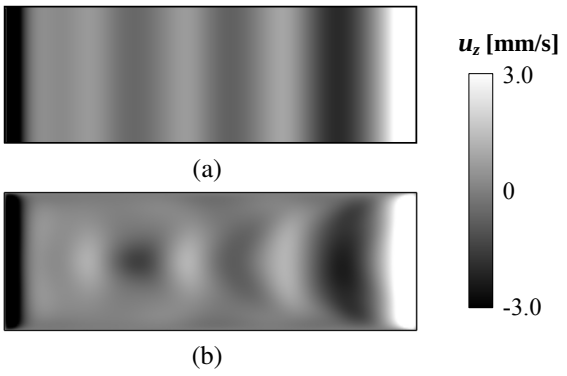

Figure 24: The velocity of the liquid in the horizontal plane $z = 1$ mm for $\Delta T = 20$ K. The vertical component u_z is shown for (a) the 2D solution and (b) the 3D solution.

heat flux through the free surface) made by previous studies based on one-sided transport models. Specifically, we found that these assumptions are satisfied in the core region of the flow, but not close to the end walls, when the convection pattern is dominated by one big recirculation zone. When convection rolls appear in the core region of the flow, the heat flux through the interface can no longer be ignored, although the other two assumptions might still hold. Unfortunately, this means that neither the results of numerical simulations nor the results of linear stability analysis based on one-sided models (i.e., essentially all theoretical results published to date) are quantitatively accurate. Although our simulations were performed for a volatile fluid (0.65 cSt silicone oil), we expect the same conclusions to hold for less volatile fluids as well. In fact, since diffusion of vapors through air greatly suppresses phase change at the interface, volatile and non-volatile fluids should have very similar behavior.

Numerically modeling the flow gave us the capability to elucidate the details of the convective patterns and both discover new phenomena and understand previously unexplained experimental observations. In particular, by investigating the structure of the boundary layers that form near the end walls of the cavity we found a counter-intuitive effect that has never been observed either in experiments or in numerical simulations using one-sided models: there is a region of evaporation close the cold end wall and a region of condensation near the hot end wall. We showed that this effect could be explained by advective heat transport in the liquid layer.

Furthermore, we derived an analytical solution for the concentration of vapor (and gas velocity) in the core region of the flow and showed that this analytical solution can be used to explain why the temperature of the free surface varies linearly with position along the direction of the applied temperature gradient, even though the temperature in the gas phase does not. This observation has been used previously in numerous numerical and analytical (e.g. linear stability) studies of the problem, but has never been justified. Together with the "single-phase" analytical solution for the velocity and temperature in the liquid layer obtained by Kirdyashkin [8] and Villers and Platten [9], this new solution provides a self-consistent analytical description of the two-phase flow away from the end walls.

In conclusion, it should be mentioned that this model can, with straightforward modifications, also describe two-phase flows in the absence of air (or at greatly reduced total pressure). This is the situation of relevance for two-phase flows in thermal management technologies (e.g., heat pipes, heat spreaders, etc.), where noncondensables are removed to minimize their effects on phase change, and will be considered in the follow-up publications.

Acknowledgments

This work is supported by the Thermal Management Program at the Office of Naval Research under Grant No. N00014-09-1-0298. We are grateful to Minami Yoda for many helpful discussions and for help with preparing the manuscript. We are also grateful to Hrvoje Jasak for help with numerical implementation of the model using OpenFOAM.

Appendix A. Grid Convergence of the Numerical Solutions

All of the numerical solutions presented in this study have achieved grid convergence and the results were presented on the finest mesh. The properties of typical meshes are summarized in Table A.3, while Table A.4 illustrates convergence for 2D simulations with $\Delta T = 10$ K and $\theta = 90°$.

	Mesh 1	Mesh 2	Mesh 3	Mesh 4
Smallest mesh size (mm)	0.5	0.25	0.125	0.0625
No. of cells in the liquid	480	1920	7680	30720
No. of cells in the gas	1440	3168	6054	10620
No. of faces along interface	96	192	384	768
Time step (s)	2×10^{-3}	1×10^{-3}	4×10^{-4}	1×10^{-4}

Table A.3: Different 2D meshes used in the mesh refinement procedure.

	Mesh 1	Mesh 2	Mesh 3	Mesh 4
Temp. range in liquid (K)	9.71	9.84	9.91	9.94
Deviation from Mesh 4 (%)	2.32	0.99	0.32	–
Max. vapor concentration (%)	4.54	4.64	4.74	4.82
Deviation from Mesh 4 (%)	5.8	3.7	1.7	–
Min. vapor concentration (%)	3.73	3.73	3.72	3.70
Deviation from Mesh 4 (%)	0.65	0.64	0.52	–
$\lvert\mathbf{u}_l\rvert$ at $x = L/2$ (mm/s)	3.50	4.55	4.92	5.01
Deviation from Mesh 4 (%)	30.1	9.2	1.8	–

Table A.4: Grid convergence of the temperature, density, and velocity fields for the numerical solutions reported in this study.

The time step is affected by many factors, such as the mesh cell size, the value of the contact angle, the temperature differential ΔT, etc. Generally, finer meshes, smaller contact angles, and greater temperature gradients require smaller time steps. Moreover, for $\theta \neq 90°$, the higher curvature of the free surface for 3D simulations, compared with 2D calculations, requires an even smaller time step. In this study, the time step used in the 2D simulations with Mesh 4 decreases from 10^{-4} s to 2.5×10^{-5} s, as θ decreases from 90° to 50°. In the 3D simulations, the time step decreases from 10^{-4} s to 10^{-5} s, as θ decreases from 90° to 50°. The total computation time increases significantly in the 3D simulations both due to smaller time steps and due to an increase (by orders of magnitude) in the total number of mesh cells. Typical computation time for a 2D simulation presented in this study is about one week on a single core of an Intel Core i7-3770K CPU, while typical computatation time for a 3D simulation is over a month, even when parallelized to use multiple (6 to 16) cores of an AMD Opteron 6300-series CPU. Unfortunately, parallelized simulations are not implemented very efficiently in OpenFOAM, so the actual speed-up for a simulation running on 16 cores is no more than 3-4.

References

[1] M. K. Smith, S. H. Davis, Instabilities of dynamic thermocapillary liquid layers. Part 1. Convective instabilities, J. Fluid Mech. 132 (1983) 119–144.

[2] M. K. Smith, S. H. Davis, Instabilities of dynamic thermocapillary liquid layers. Part 1. Surface-wave instabilities, J. Fluid Mech. 132 (1983) 145–162.

[3] M. F. Schatz, G. P. Neitzel, Experiments on thermocapillary instabilities, Annu. Rev. Fluid Mech. 33 (2001) 93–127.

[4] D. Villers, J. K. Platten, Coupled buoyancy and Marangoni convection in acetone: experiments and comparison with numerical simulations, J. Fluid Mech. 234 (1992) 487–510.

[5] C. De Saedeleer, A. Garcimartín, G. Chavepeyer, J. K. Platten, G. Lebon, The instability of a liquid layer heated from the side when the upper surface is open to air, Phys. Fluids 8 (3) (1996) 670–676.

[6] A. Garcimartín, N. Mukolobwiez, F. Daviaud, Origin of waves in surface-tension-driven convection, Phys. Rev. E 56 (2) (1997) 1699–1705.

[7] R. J. Riley, G. P. Neitzel, Instability of thermocapillarybuoyancy convection in shallow layers. Part 1. Characterization of steady and oscillatory instabilities, J. Fluid Mech. 359 (1998) 143–164.

[8] A. G. Kirdyashkin, Thermogravitational and thermocapillary flows in a horizontal liquid layer under the conditions of a horizontal temperature gradient, Int. J. Heat Mass Transfer 27 (1984) 1205–1218.

[9] D. Villers, J. K. Platten, Separation of Marangoni convection from gravitational convection in earth experiments, Phys. Chem. Hydrodyn. 8 (1987) 173–183.

[10] P. M. Parmentier, V. C. Regnier, G. Lebon, Buoyant-thermocapillary instabilities in medium-Prandtl-number fluid layers subject to a horizontal gradient, Int. J. Heat Mass Transfer 36 (1993) 2417–2427.

[11] J. F. Mercier, C. Normand, Buoyant-thermocapillary instabilities of differentially heated liquid layers, Phys. Fluids 8 (1996) 1433–1445.

[12] J. Mercier, C. Normand, Influence of the Prandtl number on the location of recirculation eddies in thermocapillary flows, Int. J. Heat Mass Transfer 45 (2002) 793–801.

[13] J. Priede, G.Gerbeth, Convective, absolute, and global instabilities of thermocapillary-buoyancy convection in extended layers, Phys. Rev. E 56 (4) (1997) 4187–4199.

[14] H. Ben Hadid, B. Roux, Buoyancy- and thermocapillary-driven flows in differentially heated cavities for low-Prandtl-number fluids, J. Fluid Mech. 235 (1992) 1–36.

[15] M. Mundrane, A. Zebib, Oscillatory buoyant thermocapillary flow, Phys. Fluids 6 (10) (1994) 3294–3306.

[16] X. Lu, L. Zhuang, Numerical study of buoyancy- and thermocapillary-driven flows in a cavity, Acta Mech Sinica (English Series) 14 (2) (1998) 130–138.

[17] V. M. Shevtsova, A. A. Nepomnyashchy, J. C. Legros, Thermocapillary-buoyancy convection in a shallow cavity heated from the side, Phys. Rev. E 67.

[18] Y. Ji, Q.-S. Liu, R. Liu, Coupling of Evaporation and Thermocapillary Convection in a Liquid Layer with Mass and Heat Exchanging Interface, Chin. Phys. Lett. 25 (2008) 608–611.

[19] H. Wang, J. Y. Murthy, S. V. Garimella, Transport from a volatile meniscus inside an open microtube, Int. J. Heat Mass Transfer 51 (2008) 3007–3017.

[20] Z. Pan, H. Wang, Symmetry-to-asymmetry transition of Marangoni flow at a convex volatizing meniscus, Microfluidics and Nanofluidics 9 (2010) 657–669.

[21] H. Wang, Z. Pan, S. V. Garimella, Numerical investigation of heat and mass transfer from an evaporating meniscus in a heated open groove, Int. J. Heat Mass Transfer 54 (2011) 30153023.

[22] R. W. Schrage, A Theoretical Study of Interface Mass Transfer, Columbia University Press, New York, 1953.

[23] P. J. Wayner, Y. K. Kao, L. V. LaCroix, The Interline heat transfer coefficient of an evaporating wetting film, Int. J. Heat Mass Transfer 19 (1976) 487–492.

[24] `http://www.openfoam.com`, 2012.

[25] Z. Tukovic, H. Jasak, A moving mesh finite volume interface tracking method for surface tension dominated interfacial fluid flow, Computers & Fluids 55 (2012) 70–84.

[26] R. LeVeque, Finite Volume Methods for Hyperbolic Problems, Cambridge University Press, Cambridge, 2002.

[27] R. I. Issa, Solution of the Implicitly Discretised Fluid Flow Equations by Operator-Splitting, J. Comp. Phys. 62 (1986) 40–65.

[28] Y. Li, R. O. Grigoriev, M. Yoda, Experimental study of the effect of non-condensables on buoyancy-thermocapillary convection in a volatile silicone oil, Phys. Fluids (2013) under consideration.

[29] J. M. Ha, G. P. Peterson, Analytical Prediction of the Axial Dryout Point for Evaporating Liquids in Triangular Microgrooves, ASME J. Heat Transfer 116 (1994) 498–503.

[30] B. Suman, P. Kumar, On the Transient Analysis of a V-Shaped Microgrooved Heat Pipe, Int. J. Heat Mass Transfer 48 (2005) 44984509.

[31] M. Markos, V. S. Ajaev, G. M. Homsy, Steady flow and evaporation of a volatile liquid in a wedge, Phys. Fluids 18 (2006) 092102.

[32] C. L. Chan, C. F. Chen, Effect of gravity on the stability of thermocapillary convection in a horizontal fluid layer, J. Fluid Mech. 647 (2010) 91–103.

[33] P. Hintz, D. Schwabe, H. Wilke, Convection in a Czochralski crucible - Part 1 : non-rotating crystal, Journal of Crystal Growth 222 (2001) 343–355.

[34] P. Gillon, G. M. Homsy, Combined thermocapillarybuoyancy convection in a cavity: An experimental study, Phys. Fluids 8 (11) (1996) 2953–2963.

[35] J. Burguete, N. Mukolobwiez, F. Daviaud, N. Garnier, A. Chiffaudel, Buoyant-thermocapillary instabilities in extended liquid layers subjected to a horizontal temperature gradient, Phys. Fluids 13 (10) (2001) 2773–2787.

[36] C. L. Yaws, Yaws' Handbook of Thermodynamic and Physical Properties of Chemical Compounds (Electronic Edition): physical, thermodynamic and transport properties for 5,000 organic chemical compounds, Knovel, Norwich, 2003.

[37] C. L. Yaws, Yaws' Thermophysical Properties of Chemicals and Hydrocarbons (Electronic Edition), Knovel, Norwich, 2009.